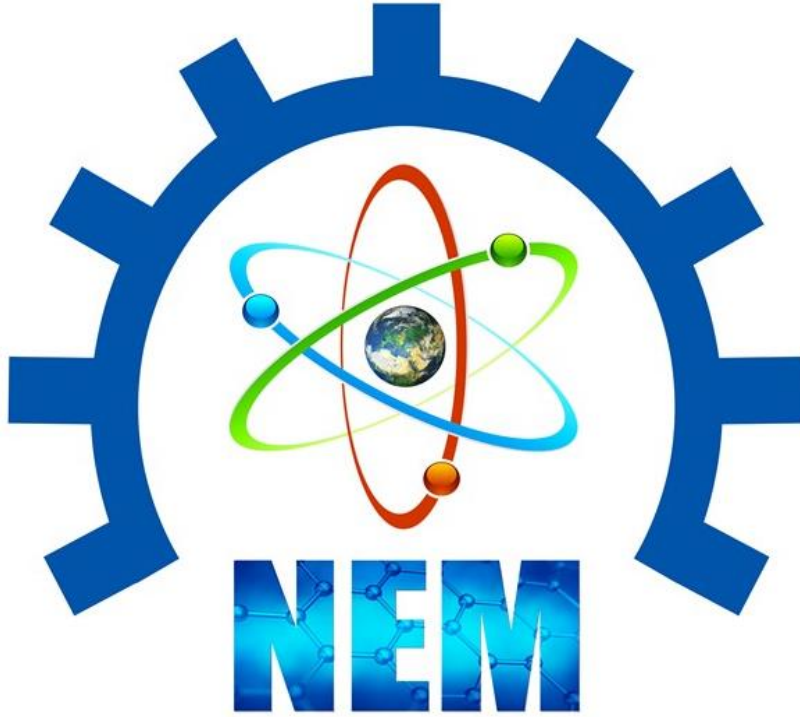# NEM 2024
FULL TEXT BOOK

4th International Natural Science, Engineering and Material Technologies Conference

September 12-14, 2024, İğneada / Kırklareli

FOREWORD

It is a pleasure for us to offer you this Book of Abstract for the 4th International Natural Science, Engineering and Material Technologies Conference (NEM 2024). Our goal was to create a platform that introduces the newest results on internationally recognized experts to local students and colleagues and simultaneously displays relevant Turkish achievements to the world. The positive feedback of the community encouraged us to proceed and transform a single event into a conference series. Now, NEM 2024 is honored by the presence of over 105 colleagues from various countries. We stayed true to the original NEM 2024 concept and accepted contributions from all fields of materials science and technology to promote multidisciplinary discussions. The focal points of the conference emerged spontaneously from the submitted abstracts: energy applications, advanced materials, electronic and optoelectronic devices, organic electronic materials, chemistry, physics, environmental science, medical science, applied and engineering science, computer simulation of organic structures, biomedical applications and advanced characterization techniques of nanostructured materials. Further fields of interest include e.g. new advanced and functional materials, advanced-functional composites, biomaterials, smart materials, dielectric materials, optical materials, magnetic materials, organic semiconductors, inorganic semiconductors, electronic materials, graphene, and more.
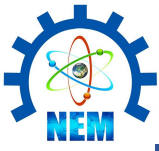
Therefore, we hope that getting first-hand access to so many new results, establishing new connections and enjoying the İğneada, Kırklareli ambience will make you feel that your resources were spent well in NEM 2024.

Our warmest thanks go to all invited speakers, authors, and contributors of NEM 2024 for accepting our invitation, visiting İğneada, Kırklareli and using NEM 2024 as a medium for communicating your research results.

We hope that you will enjoy the conference and look forward to meeting you again in one of the forthcoming **NEM 2025** event.

Best regards,
Conference President

Assoc. Prof. Burhan COŞKUN

Editor:

Assoc. Prof. Burhan COŞKUN

Published, September-2024

nem2024.klu.edu.tr

nem@klu.edu.tr

COMMITTEE

HONORARY PRESIDENT

Prof. Dr. Bülent ŞENGÖRÜR (Rector of Kırklareli University)

CONFERENCE PRESIDENT

Assoc. Prof. Burhan COŞKUN (Kırklareli University)

ORGANIZING COMMITTEE

Prof. Dr. Cemile ÖZCAN / Kırklareli University

Prof. Dr. Meryem ÇAMUR DEMİR- Kırklareli University

Prof. Dr. Sermet KOYUNCU / Çanakkale Onsekiz Mart University

Prof. Dr. Serpil AKÖZCAN / Kırklareli University

Assoc. Prof. Ayşegül DERE / Fırat University

Assoc. Prof. Dr. Berna AKGENÇ HANEDAR / Kırklareli University

Assoc. Prof. Dr. Fatma KURŞUN BAYSAK / Kırklareli University

Assoc. Prof. Dr. H. Hale KARAYER / Kırklareli University

Assoc. Prof. Dr. Mehmet Mümin KOÇ / Kırklareli University

Assoc. Prof. Dr. Mustafa KURBAN / Ankara University

Assoc. Prof. Dr. Nurdan KURNAZ YETİM / Kırklareli University

Assoc. Prof. Dr. Özge Kılıçoğlu MEHMETCİK / Marmara University

Assoc. Prof. Dr. Selin ÖZDEN / Kırklareli University

Dr. Instructor Bahadır BEKÂR / Trakya University

Dr. Instructor Nihat AKKURT / Kırklareli University

Dr. Instructor Ufuk PAKSU / Kırklareli University

Dr. Çiğdem Ş. GÜÇLÜ / Gazi University

Lecturer Z. Açelya KURT / Kırklareli University

SCIENTIFIC COMMITTEE

Prof. Dr. Abdel Salam Hamdy MAKHLOUF / University of Texas / UNITED STATES

Prof. Dr. Abdullah G. AL-SEHEMI / King Khalid University / SAUDI ARABIA

Prof. Dr. Ahmed A. ALGHAMDI / King Abdulaziz University / SAUDI ARABIA

Prof. Dr. Ali DİŞLİ / Gazi University / TÜRKİYE

Prof. Dr. Asa H. BARBER / London South Bank University / UNITED KINGDOM

Prof. Dr. Azar AHMADOV / Baku State Gazi University / AZERBAIJAN

Asst. Prof. Bahadır BEKAR / Trakya University / TÜRKİYE

Assoc. Prof. Dr. Bayram ÇETİN / Kırklareli University / TÜRKİYE

Prof. Dr. Burç MISIRLIOĞLU / Sabancı University / TÜRKİYE

Asst. Prof. Burhan CEYLAN / Harran University / TÜRKİYE

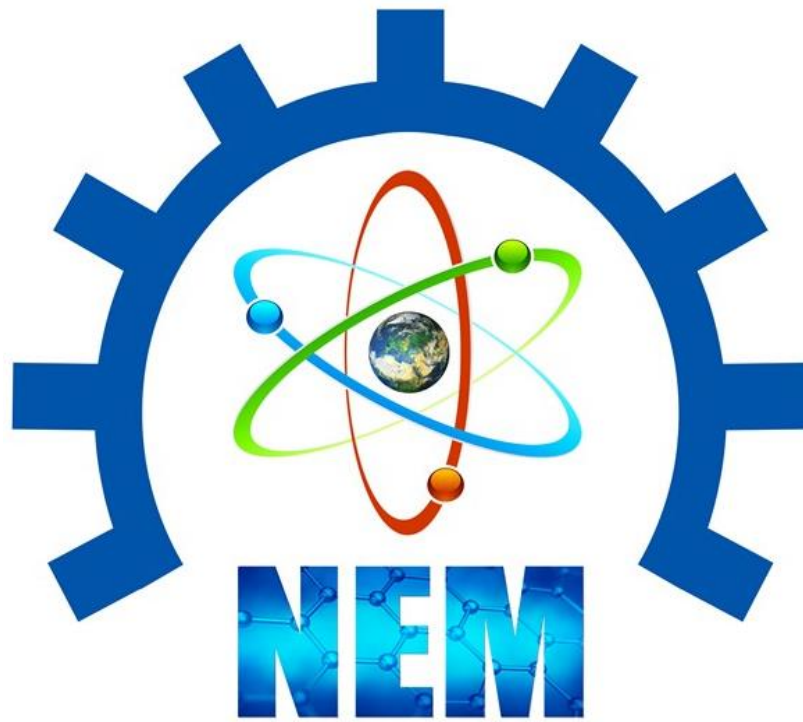Prof. Dr. Canan AKSU CANBAY / Fırat University / TÜRKİYE

Prof. Dr. Chung GWIY-SANG / Ulsan University / KOREA

Prof. Dr. Denis NIKA / Moldova University / MOLDOVA

Asst. Prof. Dr. Devrim ÖZDAL / European University of Lefke / North Cyprus

Prof. Dr. Dilek NARTOP / Düzce University / TÜRKİYE

Prof. Dr. Elias STATHATOS / Tecnological-Educational Institute of Patras / GREECE

Prof. Dr. Elizabeth BLACKBURN / University of Birmingham / UNITED KINGDOM

Asst. Prof. Erdinç KESKİN / Kırklareli University / TÜRKİYE

Asst. Prof. Evren ÇAĞLAER / Kırklareli University / TÜRKİYE

Assoc. Prof. Harun URAN / Kırklareli University / TÜRKİYE

Prof. Dr. Hatice ÖĞÜTCÜ / Kırsehir Ahi Evran University / Türkiye

Assoc. Prof. İsmail KILIÇ / Kırklareli University / TÜRKİYE

Assoc. Prof. Macide CANTÜRK RODOP / Yıldız Technical University / TÜRKİYE

Prof. Dr. Müjdat ÇAĞLAR / Eskişehir Anadolu University / TÜRKİYE

Prof. Dr. Mustafa ERKOVAN / Beykoz University / TÜRKİYE

Assoc. Prof. Mustafa KURBAN / Ahi Evran Gazi University / TÜRKİYE

Assoc. Prof. Naim ASLAN / Munzur University / TÜRKİYE

Prof. Dr. Niyazi ÖZDEMİR / Fırat University / TÜRKİYE

Prof. Dr. Numan AKDOĞAN / Gebze Technical University / TÜRKİYE

Assoc. Prof. Nur P. AYDINLIK / Cyprus International University / NORTH CYPRUS

Prof. Dr. Ömer Suat TAŞKIN / Istanbul University / TÜRKİYE

Prof. Dr. Ram K. GUPTA / Pittsburg State University / UNITED STATES

Prof. Dr. Raşit TURAN / Middle East Technical University / TÜRKİYE

Prof. Dr. S. MANSOURI / University of Gabès / TUNUSIA

Assoc. Prof. Sinan SEZEK / Atatürk University / TÜRKİYE

Asst. Prof. Sena Esen BAYER KESKİN / Kırklareli University / TÜRKİYE

Asst. Prof. Sencer Süreyya KARABEYOĞLU / Kırklareli University / TÜRKİYE

Assoc. Prof. Dr. Süleyman AŞIR / Near East University / NORTH CYPRUS

Assoc. Prof. Taner DAŞTAN / Cumhuriyet University / TÜRKİYE

Prof. Dr. Tarık ASAR / Gazi University / TÜRKİYE

Prof. Dr. W. Aslam FAROOQ / King Saud University / SAUDI ARABIA

Prof. Dr. Yasemin BAKIRCIOĞLU KURTULUŞ / Trakya University / TÜRKİYE

Dr. Zöhre GÖRÜNMEZ GÜNGÖR / Kırklareli University / TÜRKİYE

FULL TEXT PRESENTATIONS

FULL TEXT PRESENTATIONS

MAXIMUM POWER POINT TRACKING FOR A PHOTOVOLTAIC PANEL USING ARTIFICIAL NEURAL NETWORK

Ç. Yeşil[1], S. Kılınç[2]

[1]*The Graduate School of Natural and Applied Sciences, Dokuz Eylül University, İzmir, TÜRKİYE*
[2]*Department of Electrical and Electronics Engineering, Faculty of Engineering, Dokuz Eylül University, İzmir, TÜRKİYE*

E-mail: caglar.yesil@deu.edu.tr

In this paper, the design and simulation results of a photovoltaic (PV) system operating at its maximum power point (MPP) using MATLAB-Simulink are presented. The parameters of a 20-Watt PV panel are used in the buck converter design. A feedforward neural network is implemented for maximum power point tracking (MPPT). The neural network features an input layer with three inputs, three hidden layers with ten neurons each, and a single output layer. This architecture is selected to enhance the accuracy and responsiveness of the MPPT algorithm, especially under varying environmental conditions. The system is primarily designed as a battery charger for a 12-Volt lead-acid battery. The performance of the system is tested with simulations using MATLAB-Simulink. These simulations focus on accuracy of the MPP tracking and fast response to environmental changes and the stability of the output voltage under dynamic conditions. The results demonstrate that the neural network-based MPPT effectively optimizes the power transfer and ensures a smooth battery charging process.

Keywords: Maximum power point, Neural network, Solar energy, Battery charging

1. INTRODUCTION

In recent years, the importance of clean energy has clearly increased driven by the dramatic rise in demand for fossil fuels [1]. Solar energy systems have become one of the most popular ways among various clean energy solutions and are now widely used in many countries [2]. As industries grow and populations increase, the need for electricity increases, leading to more efforts to improve the efficiency of energy production.

Despite their many benefits solar energy systems face challenges because of their nonlinear characteristics and dependence on environmental conditions like temperature and irradiance. To increase efficiency, it is important to operate the system at its Maximum Power Point (MPP). This is where Maximum Power Point Tracking (MPPT) methods come in. MPPT algorithms constantly adjust the electrical operating point of the PV system to ensure that it operates at the MPP. The Maximum Power Point methods have been studied and applied in many ways in the literature [3-6]. Neural network-based MPPT methods have been frequently used and developed. Various neural network structures have been explored and documented in MPPT applications [7,8].

In this study, it is aimed to establish a battery charging system that reaches the MPP using neural networks. Neural network-based MPPT addresses the challenges posed by the variability of solar energy and contributes to the development of more reliable and intelligent energy management systems. The insights gained from this approach could support the wider adoption of clean energy technologies, leading to more efficient solar energy solutions.

2. SYSTEM COMPONENTS AND METHODOLOGY

This section provides a detailed overview of the fundamental components and methodologies used in our photovoltaic (PV) system. It includes descriptions of the PV panel, converter, battery, and artificial neural network (ANN), highlighting their roles and interactions within the system. Understanding these components is crucial for comprehending the overall design and functionality of the MPPT solution.

2.1 Photovoltaic Model

Photovoltaic cells (Figure 1(a)) are structures that convert sunlight into electrical energy through the use of semiconductor materials. This conversion occurs because of the photovoltaic effect. Photovoltaic cells can be modelled using components of an electrical circuit. The model includes a diode, a current generator that produces current from light, and two resistors, one in series and the other in parallel. Photovoltaic panels (Figure 1(b)) are formed by connecting photovoltaic cells in series or parallel configurations. Figure 2 shows us the basic PV panel equivalent circuit. The current-voltage (I-V) characteristic of PV panel described in Equation (1) [9].
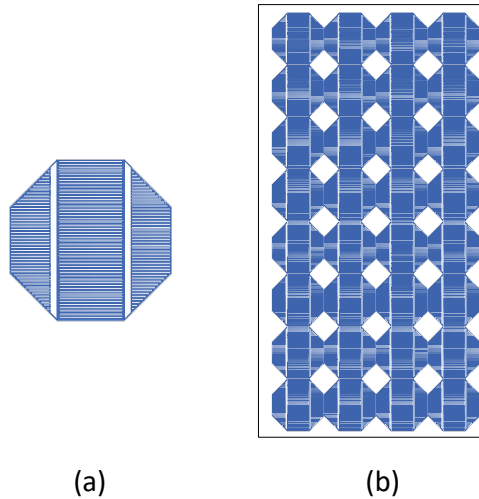
(a)   (b)

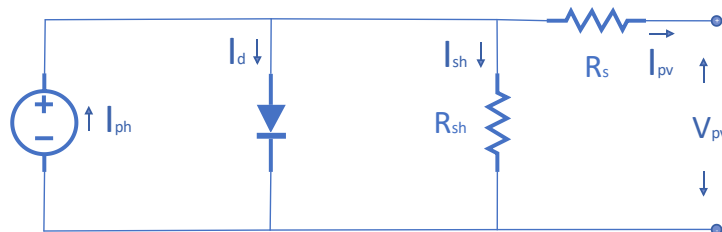**Figure 1.** a) Photovoltaic cell b) Photovoltaic panel [9]

Figure 2. Single diode model for PV panel

3

$$I = I_{ph} - I_o \left[exp\left(\frac{q(V + IR_s)}{\gamma kT}\right) - 1 \right] - \frac{V + R_s I}{R_{sh}} \qquad (1)$$

where I is the output current of PV panel (in A), I_{ph} is the photo generated current (in A), I_o is the diode saturation current (in A), q is the charge of an electron (1.602×10^{-19} C), V is the output voltage (in V), R_s is the series resistance (in Ω), R_{sh} is the shunt resistance (in Ω), n is the ideality factor of the diode (typically between 1 and 2), k is the Boltzmann constant (1.381×10^{-23} J/K), T is the cell temperature (in Kelvin) and γ is the ideality factor.

In this study, a 20W PV panelis used to supply our system. The specifications of the PV panel are given in Table 1.

Table 1. PV panel specifications

Parameter	Value
Maximum Power	20.19 W
Maximum Voltage	17.58 V
Maximum Current	1.15 A
Open Circuit Voltage	21.7 V
Short Circuit Current	1.26 A
Ideality Factor	1.78
Shunt Resistance	368.4 Ω
Series Resistance	1.22 Ω

2.2 Buck Converter Design

Recent studies in photovoltaic systems often employ boost converters, which increase the voltage from the PV panel to a higher level suitable for various applications [10,11]. However, in this study the use of a buck converter is more appropriate due to voltage compatibility. The output of the PV panel voltage is higher than the required battery charging voltage (12V). Buck converter effectively steps down the voltage to match the battery voltage requirements. Buck converter voltage conversion ratio formula is given in Equation (2).

$$V_o = D.V_{in}$$

(2)

where V_o is the output voltage, V_{in} is the input voltage of buck converter and D is the duty cycle, defined as the ratio of the time the switch is on during the total switching period. Schematic diagram of buck converter can be seen in Figure 3. The designed buck converter has 905.3 µH inductor (L), 409.79 µF capacitor (C).
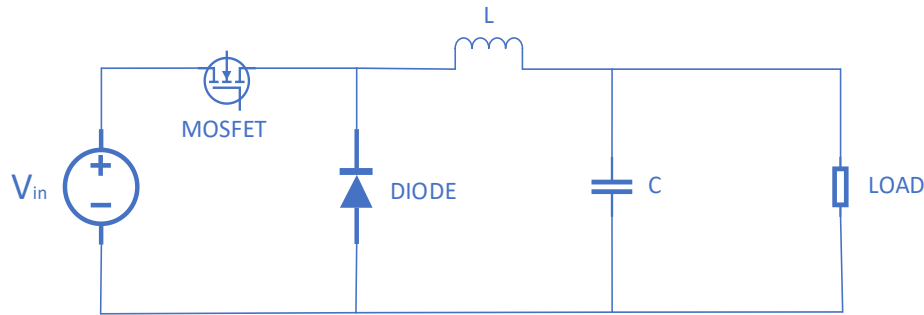

Figure 3. Buck converter schematic

2.3 Lead-acid Battery

In 2013, Yılmaz and Krein [12] reported different battery charger topologies of electrical vehicles. Lead-acid batteries are widely used in the electric vehicle industry and many other sectors due to their reliability and robustness. Lead acid batteries are known for their long lifespan, cost-effectiveness and recyclability. Recycle rate of lead acid batteries are approximately 99% [13]. In this study, lead-acid battery is used. The battery is choosen 12V and 5Ah.

2.4 Artificial Neural Network

There are numerous types of neural network MPPT algorithms in the literature [7]. In this study, we employed an Artificial Neural Network to predict the output voltage of PV panel under varying conditions of irradiance (W/m²) and temperature (°C). The ANN model is developed and trained using MATLAB.

The dataset, which consists of 1000 samples, is gathered from Terrasas Solar Array Simulator program by AMETEK [14] with irradiance ranging from 1 to 1000 W/m² and temperature from 15 to 40°C. Dataset randomly splited into training (60%), testing (20%) and validation (20%) sets.

A Feedforward Neural Network (FFNN) architecture is used in this work. The system has three inputs (irradiance, temperature, PV panel current), one output (reference voltage) and three hidden layers with 10 neurons each. Sigmoid function is used as activation function. Mean Squared

5

Error (MSE) is used to evaluate the performance of the network. The training algorithm is Levenberg-Marquardt algorithm. Simplified Neural Network architecture is shown in Figure 4.
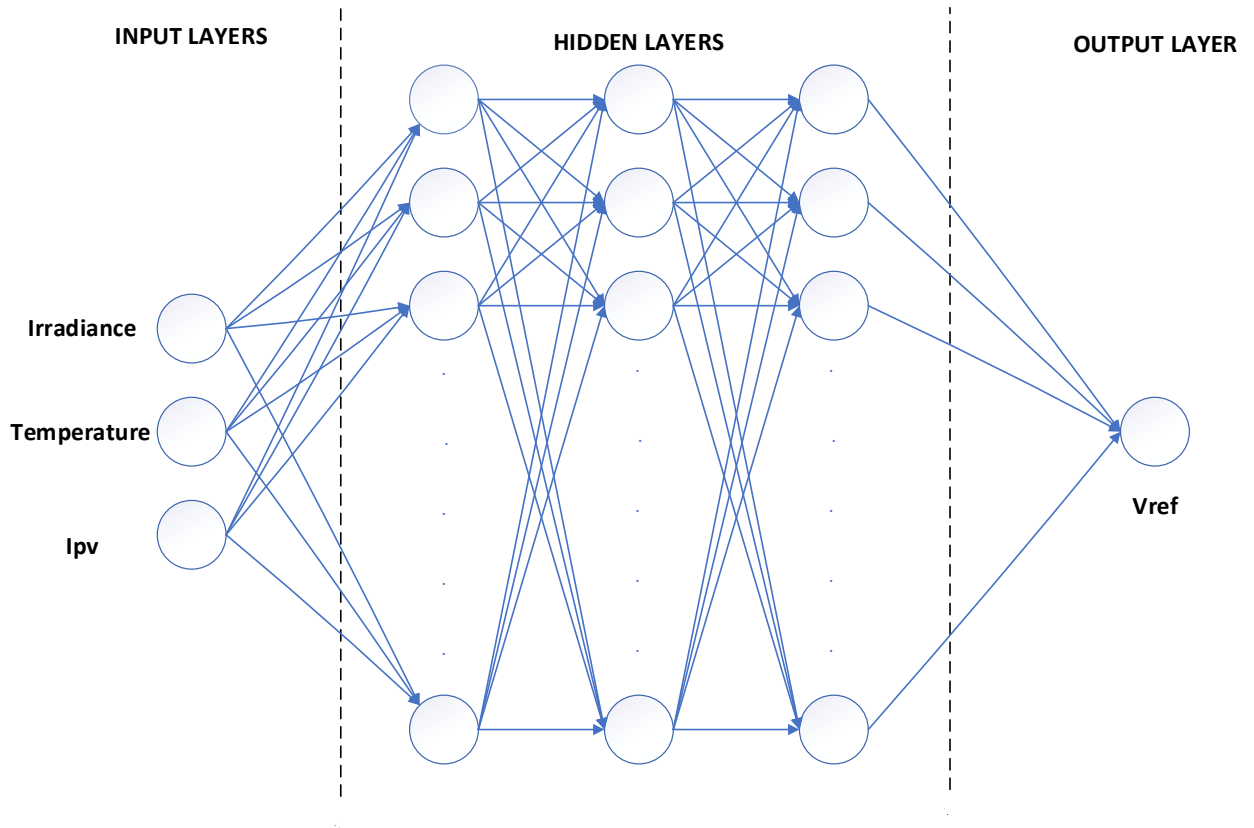
Figure 4. Simplified neural network architecture

When the system is set up, the PV panel starts producing voltage (V_{pv}) and current (I_{pv}) as a result of irradiance and temperature. The irradiance, temperature, and Ipv information are fed into the neural network, which outputs the V_{ref} value. The generated V_{ref} value is compared with V_{pv} and fed into the PI controller block. The signal resulting from the PI controller is then compared with a sawtooth signal of 1 V amplitude and 10 kHz frequency. The resulting waveform is the PWM signal used to drive the MOSFET in the buck converter. The PWM signal adjusts the MOSFET's switching frequency according to the irradiance, temperature, and current conditions, ensuring that the battery is charged at the maximum power point. Figure 5 represents the working principle of the system, which is adopted from the work in [5].
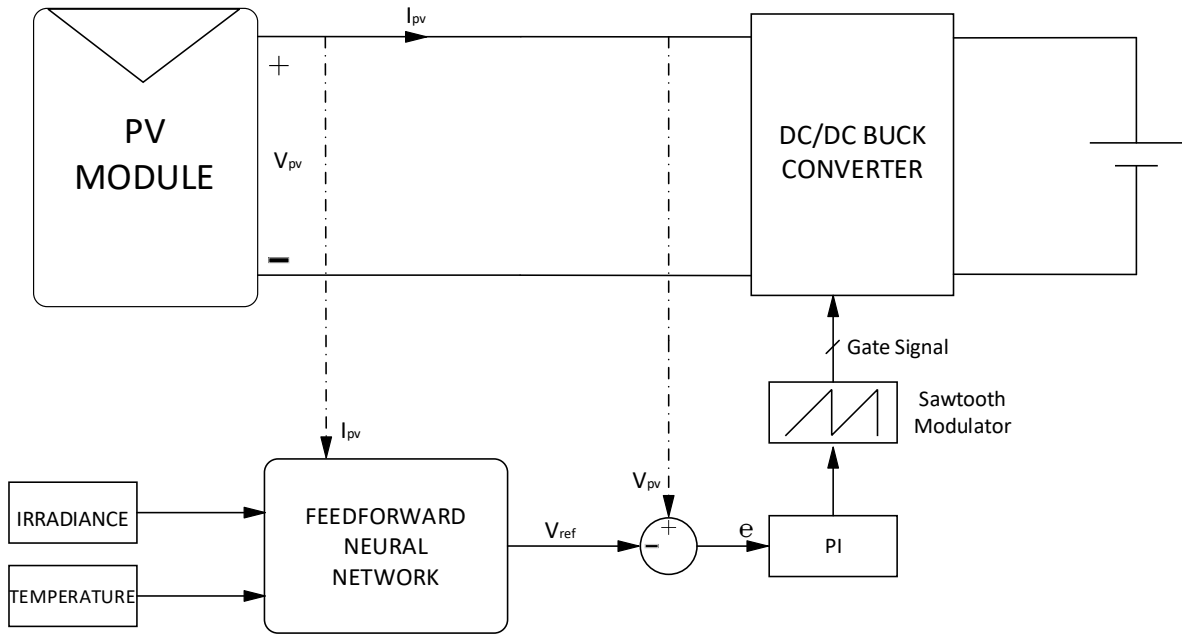
Figure 5. System work principle [5]

3. RESULTS

In this section, simulation results of the system are given. Figure 6 illustrates the MPPT system on MATLAB/Simulink. The neural network training process is utilized with MATLAB software and the training results and performance of the system are shown in Figure 7. Using the PV panel values from Table 1 and the operating principle depicted in Figure 5, the system is established and operated, achieving the MPPT values.

Figure 6. MATLAB/Simulink model of the MPPT system
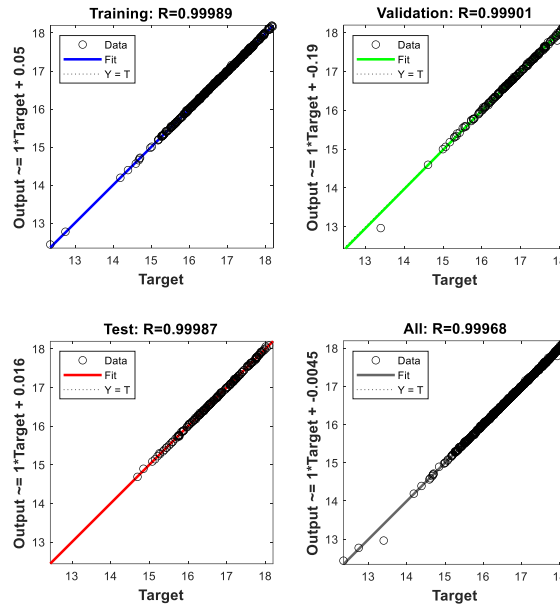
Figure 7. Regression results of neural network

Figure 7 depicts the success rate of the neural network learning. The regression graph resulting from the artificial neural network simulation in MATLAB expresses the relationship between the outputs predicted by the neural network and the actual target values. An R value close to 1 indicates that the model's predictions are very accurate. R value close to 0 indicates that the model's predictions are unreliable. Our overall R value is 0.99968, which means very accurate.

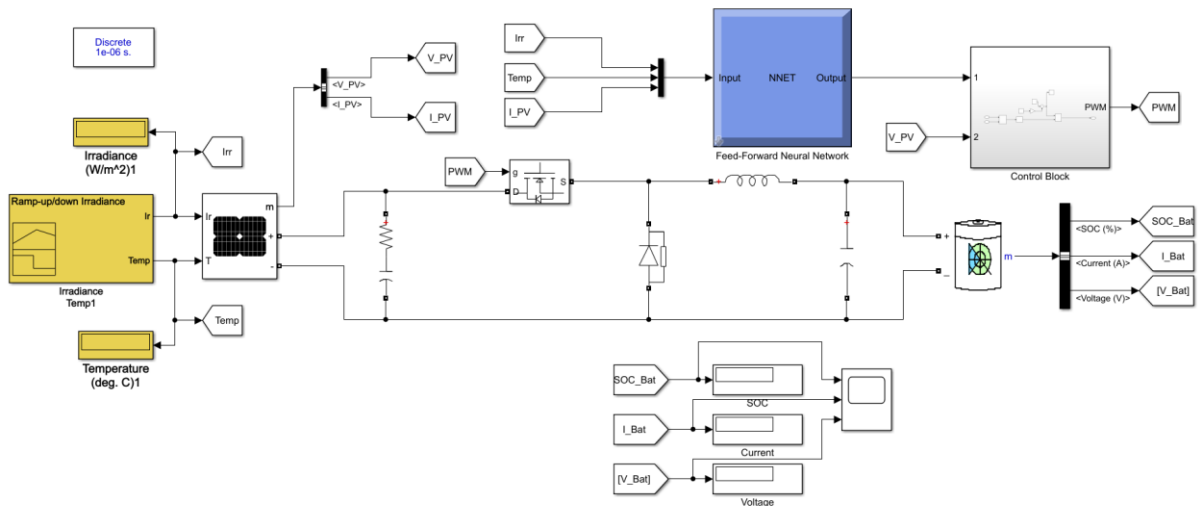One of the objectives of this study, battery charging, is accomplished using the neural network Maximum Power Point Tracking (MPPT) method. It is observed that the battery charging process is successfully executed.

In 2020, Zecevic and Bolevski [8] conduct a study on MPPT control using neural networks. Building on their approach, we conduct our simulation under identical irradiance and temperature conditions, with the results summarized in Table 2. The table shows the prediction error of MPP across various irradiance levels. As observed, the prediction error is high under low irradiance conditions. However, as the irradiance levels increase, the prediction error decreases. This trend indicates that the system's accuracy in closely approximating the MPP improves at higher irradiance levels.

Table 2. Prediction error rate

Irradiance (W/m²)	Prediction Error (%)
110.2	1.86
132.2	1.7
225.1	1.3
260.5	1.53
302.9	1.57
369.9	1.27
409.7	1.07
523.5	0.72
613.3	0.48
653.8	0.44
713.4	0.25
859.5	0.03
946.8	0.003
1007.1	0.003
1084.3	0.012

4. CONCLUSION

This research successfully demonstrates charging a battery at the maximum power point by controlling solar energy systems with artificial neural networks. The neural network method used in the system results in low error margins and ensures stable and reliable operation, especially at high irradiation levels. Artificial neural network is trained using PV panel data produced with AMETEK's TERRASAS software, via MATLAB. Comprehensive simulations conducted in Simulink confirms that the system operates quickly and efficiently under varying conditions. This research presents an effective approach for solar energy usage and operation at the maximum power point, contributing to the advancement of renewable energy technologies.

REFERENCES

[1] Nejat P, Jomehzadeh F, Taheri MM, Gohari M, Majid MZA. "A global review of energy consumption, CO2 emissions and policy in the residential sector (with an overview of the top ten CO2 emitting countries)". Renewable and Sustainable Energy Reviews, 43, 843-862, 2015.

[2] International Renewable Energy Agency. "Renewable energy statistics 2023". https://www.irena.org/publications/2023/Jul/Renewable-Energy-Statistics-2023 (25.06.2024).

[3] Baba AO, Liu G, Chen X. "Classification and Evaluation Review of Maximum Power Point Tracking Methods". Sustainable Futures, 2, 100020, 2020.

[4] Katche ML, Makokha AB, Zachary SO, Adaramola MS. "A Comprehensive Review of Maximum Power Point Tracking (MPPT) Techniques Used in Solar PV Systems". Energies, 16(5), 2023.

[5] Durbaba E, Akpınar E, Balıkçı A, Azizoğlu BT, Kocamış AE. "Fast Prototyping of A Photovoltaic System by Using DSP in MATLAB Simulation Loop". IECON 2019 - 45th Annual Conference of the IEEE Industrial Electronics Society, Lisbon, Portugal, 14-17 October 2019.

[6] Podder AK, Roy NK, Pota HR. "MPPT methods for solar PV systems: a critical review based on tracking nature". The Institution of Engineering and Technology Renewable Power Generation, 13(10), 1615-1632, 2019.

[7] Elobaid LM, Abdelsalam AK, Zakzouk EZ. "Artificial neural network-based photovoltaic maximum power point tracking techniques: a survey". The Institution of Engineering and Technology Renewable Power Generation, 9(8), 1043-1063, 2015.

[8] Zecevic Z, Rolevski M. "Neural Network Approach to MPPT Control and Irradiance Estimation" Applied Sciences, 10, 5051, 2020.

[9] Olayiwola TN, Hyun SH, Choi SJ. "Photovoltaic Modeling: A Comprehensive Analysis of the I–V Characteristic Curve". Sustainability, 16, 432, 2024.

[10] Das C, Mandal K, Roy M. "Design of PV Emulator Fed MPPT Controlled DCDC Boost Converter for Battery Charging". 2020 IEEE First International Conference on Smart Technologies for Power, Energy and Control, Nagpur, India, 25-26 September 2020.

[11] Hussein HA, Mahdi AJ, Abdul-Wahhab TM. "Design of a Boost Converter with MPPT Algorithm for a PV Generator Under Extreme Operating Conditions". Engineering and Technology Journal, 39(10), 1473-1480, 2021.

[12] Yılmaz M, Krein PT. "Review of Battery Charger Topologies, Charging Power Levels, and Infrastructure for Plug-In Electric and Hybrid Vehicles". IEEE Transactions on Power Electronics, 28(5), 2151-2169, 2013.

[13] Yanamandra K, Pinisetty D, Daoud A, Gupta N. "Recycling of Li-Ion and Lead Acid Batteries: A Review". Journal of the Indian Institute of Science, 102(1), 281-295, 2022.

[14] Elgar Terrestrial Solar Array Photovoltaic Simulator - Terrasas by AMETEK. Available at: https://www.programmablepower.com/products/engineered-systems/terrasas-ets-series

CALCULATION OF OPTICAL TRANSITIONS IN AN ARROWHEAD-SHAPED QUANTUM WIRE DEPENDING ON THE ELECTRIC AND LASER FIELD

B. Bekar

Keşan Vocational School, Trakya University, Keşan, Edirne, TÜRKİYE

bahadirbekar@trakya.edu.tr

In this study, we considered an arrowhead-shaped AlGaAs/GaAs quantum wire. We used the finite difference method under the effective mass approximation to calculate eigenvalues and eigenvectors. We applied an external electric field and a laser field to the system. We tried to show the change in optical transition coefficients when there is and without the effect of external fields.

Keywords: Quantum wire, electric field, laser field, optic apsorbtion coefficient

1. INTRODUCTION

With the discovery of semiconductors in the early 20th century, a fast race was started in terms of technology. Semiconductors are juxtaposed to form diodes, LEDs, transistors. It has been used in many areas such as solar cells[1-9]. One of these areas of use has been optical devices. E. Kasaoğlu et al. evaluated linear and nonlinear optical transition coefficients under the effective mass approximation in quantum wells with Rosen-Mosen type potential; They calculated it under the effects of electric field, pressure, temperature, magnetic field, etc[10-13]. E. Niculescu et al. also calculated the energy eigenvalues of wave functions in intense laser field quantum wells and wires[14-16]. On the electric field i. Many publications have been made by I.Erdoğan et al. and they have shown the effects of self-polarization on energy, eigenvalues and eigenvectors of the structure under external fields[17-22]

In this study, we investigated the effects of linear and nonlinear absorption and refractive index in the arrowhead-shaped quantum wire depending on the electric field and laser field.

2. MATERIAL AND METHODS

In this study, we discussed the AlGaAs/GaAs quantum wire in the form of an arrow. We used the finite difference method under the effective mass approximation for our calculations. We took the potential profile of the structure as shown in Figure 1.
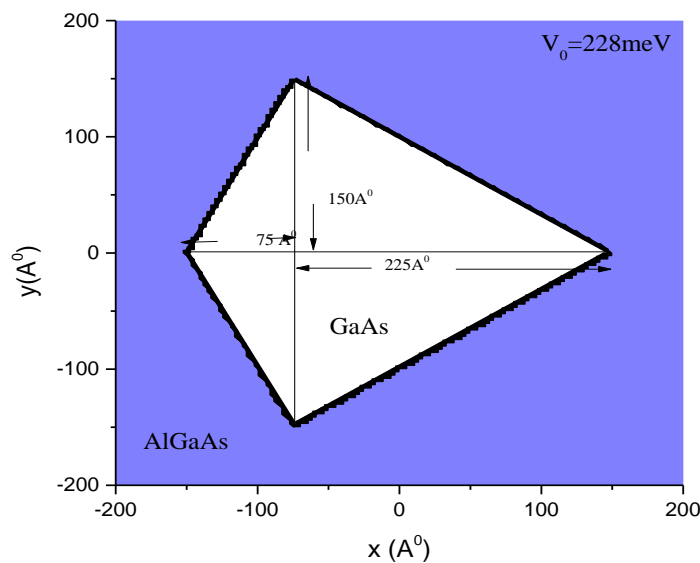

Figure 1: Potential profile of an arrow-shaped quantum wire

The time-dependent Schrödinger equation for the ASQW can be written as

$$\left\{\frac{1}{2m^*}[p_\perp + eA(t)]^2 + V(x,y) + |e|.F.x\right\}\psi(x,y,t) = i\hbar\frac{\partial}{\partial t}\psi(x,y,t) \qquad (1)$$

Where $p_\perp$ is the momentum of the electron on the (x,y) plane, e is the electron charge when the laser field is off , m* is the effective mass of the electron, F is he electric field strength. The laser vector potential is given as $A(t) = \hat{x}A_0\cos(wt)$, $\hat{x}$ being the unit vector along the x-axis. By applying the time-dependent translation x→x+$\alpha_0$sin(wt) and performing the unitary Kramers-Henneberger transformation can be rewritten as [14,16,22]

$$\left[-\frac{\hbar^2}{2m^*}\left(\frac{\partial^2}{\partial x^2} + \frac{\partial^2}{\partial y^2}\right) + \widetilde{V_{dr}}(x,y) + |e|.F.x\right]\tilde{\psi}(x,y) = E\tilde{\psi}(x,y) \qquad (2)$$

$$\tilde{V}_{dr}(x,y) = \frac{w_D}{2\pi}\int_0^{2\pi/W_D} V(x,y,t).dt = \frac{1}{2\pi}\int_0^{2\pi} V(x+\alpha_0\sin\theta,y).d\theta \qquad (3)$$

Here $\widetilde{V_{dr}}$ the laser is called the dressed potential and is calculated in the form. $\alpha_0 = \frac{e.A_0}{m^*.w_D}$ the laser dressed parameter, $\frac{2\pi}{w_D}$ is the period of the laser field[14]. E_f and E_i describe the energies of the last and first states respectively, E_{if} is the energy difference between these states, it is defined as

$$E_{if} = E_f - E_i \qquad (4)$$

M_{if} dipole matrix element is calculated from the following equation.

$$M_{if} = \left|< \psi_i|e.x|\psi_f >\right| \qquad (5)$$

Where e is the electron charge. ψ_i wave function in the first state , ψ_f is the wave function in the last state. ħω in the equations is the energy of the incident photon, σ is the carrier density in the system, , $n_s = \sqrt{\varepsilon}$ is the refractive index of the system, c is the speed of light in a vacuum, , ε_0 is the dielectric constant, τ_{in} is the relaxation time. I is the optical intensity of the light applied to the system from the outside.

$$\beta^{(1)}(\omega) = \frac{\sigma}{c\varepsilon_0 n_s}\frac{\hbar\omega|M_{if}|^2/\tau_{in}}{(E_{if}-\hbar\omega)^2+(\hbar/\tau_{in})^2} \qquad (6)$$

13

$$\beta^{(3)}(\omega) = -\frac{2\sigma}{(c\varepsilon_0 n_s)^2}\frac{\hbar\omega I|M_{if}|^4/\tau_{in}}{[(E_{if}-\hbar\omega)^2+(\hbar/\tau_{in})^2]^2}$$

$$x\left[1-\right.$$

$$\left|\frac{M_{ff}-M_{ii}}{2M_{if}}\right|^2\frac{(E_{if}-\hbar\omega)^2-(\hbar/\tau_{in})^2+2E_{if}(E_{if}-\hbar\omega)}{E_{if}^2+(\hbar/\tau_{in})^2}\right] \tag{7}$$

The total absorption coefficient β (ħω,I) is as in the equation below [14,22].

$$\beta(\omega,I) = \beta^{(1)}(\hbar\omega) + \beta^{(3)}(\hbar\omega,I) \tag{8}$$

Refractive index changes involving linear and nonlinear terms are calculated from the following equations, respectively[14,22].

$$\frac{\Delta n^{(1)}(\omega)}{n_s} = \frac{\sigma}{2\varepsilon_0 n_s^2}\frac{|M_{if}|^2(E_{if}-\hbar\omega)}{(E_{if}-\hbar\omega)^2+(\hbar/\tau_{in})^2} \tag{9}$$

$$\frac{\Delta n^{(3)}(\omega,I)}{n_s} = -\frac{\sigma}{c\varepsilon_0^2 n_s^3}\frac{I|M_{if}|^4(E_{if}-\hbar\omega)}{[(E_{if}-\hbar\omega)^2+(\hbar/\tau_{in})^2]^2}$$

$$x\left\{1-\left|\frac{M_{ff}-M_{ii}}{2M_{if}}\right|^2\frac{E_{if}(E_{if}-\hbar\omega)^2-\left(\frac{\hbar}{\tau_{in}}\right)^2(3E_{if}-2\hbar\omega)}{\left[E_{if}^2+\left(\frac{\hbar}{\tau_{in}}\right)^2\right](E_{if}-\hbar\omega)}\right\} \tag{10}$$

$$\frac{\Delta n(\hbar\omega,I)}{n_s} = \frac{\Delta n^{(1)}(\hbar\omega)}{n_s} + \frac{\Delta n^{(3)}(\hbar\omega,I)}{n_s} \tag{11}$$

3. RESULTS AND DISCUSSION

In the calculations, the effective mass $m^* = 0.0665m_0$ for the whole structure and $\varepsilon_s = 12.58\varepsilon_0$ and $\varepsilon_\infty = 10.9\varepsilon_0$ dielectric permeability of the medium were taken as $V_0 = 228$meV, the electron density in the system $\sigma = 3\times10^{22}m^{-3}$, the refractive index for GaAs, $n_s = \sqrt{\varepsilon}$ and the relaxation time between the inner bands $\tau_{in} = 5$ps[22]. The optical density of the light applied to the system from the outside is $I = 0.05$MW/cm^2. First, we

applied an electric field in the x-direction, and we discussed this in two sections. We also showed figure2 in a single graph, in the –x–direction and in the +x- direction. The potential profile is symmetrical in the x- direction and antisymmetric in the y-direction. After this explanation, when we look at figure 2, there is an increase in the base state energy (E_0) from F=-100kV/cm to F=-50 kV/cm, while there is a decrease after this value. It has reached the intersection of F≈10kV/cm at the first excited and second excited energy levels. In Figure 3, all energy levels in the range of F=-100kV/cm -0 and F=0-100kV/cm are symmetry due to symmetry. It has a similar energy characteristic as Figure 2.The first energy level showed an upward trend up to F=0, while the second excited energy level showed an upward trend at F=0.

Figure2: Variation of the first three energy levels depending on the electric field applied in the x and y-directions

Figure 3 is a repetition of what we did to the structure for the electric field. We applied an intense laser light polarized in the x-direction vertically on the potential profile we used (straight line). Then we applied intense laser light polarized in the y- direction (dashed line). When we looked at the graph of the ground state and first evoked energy

levels, we saw that both energy levels were the same and exhibited an increasing energy profile. At the second level of arousal, we saw very little difference. We found that the energy level of the laser light polarized in the X-direction was slightly higher. An increase in the energies of both energy lines was observed with the intensity of the laser light. The application of laser light in different directions did not lead to much change in energy levels. Figure 4 shows the effect of intense laser light on the structure when laser light polarized in the x and y- directions is applied to the quantum wire in figure 1.
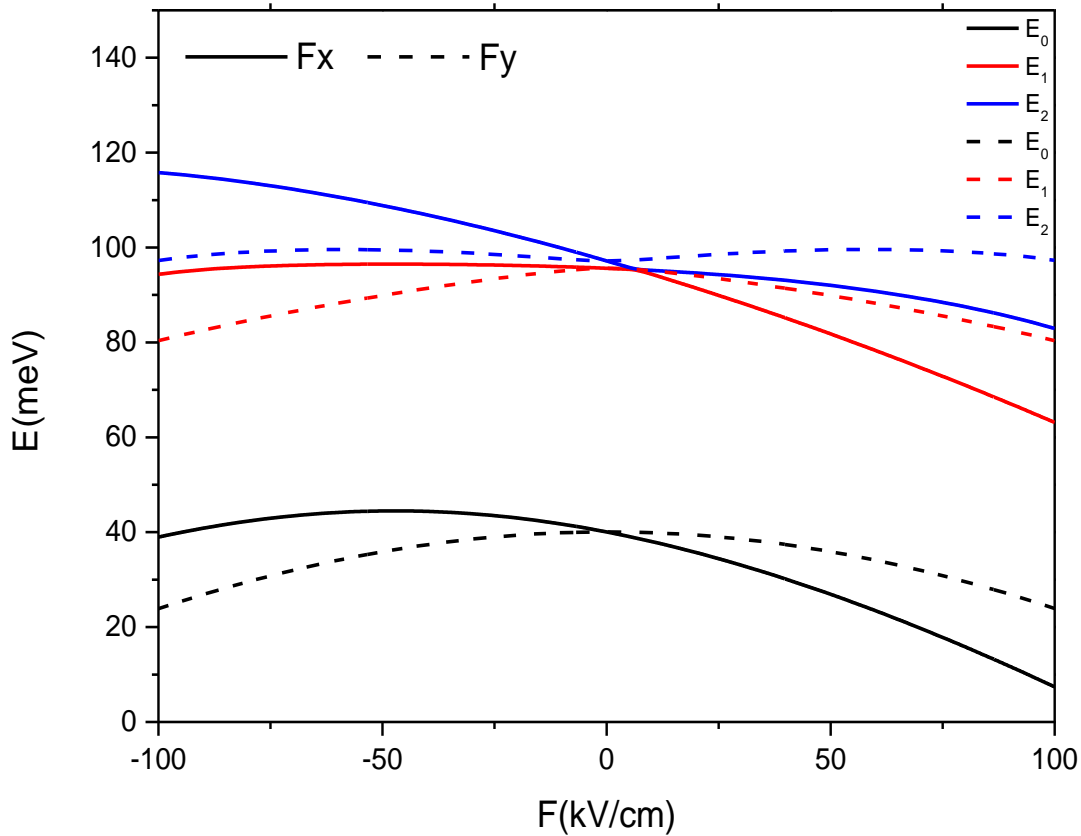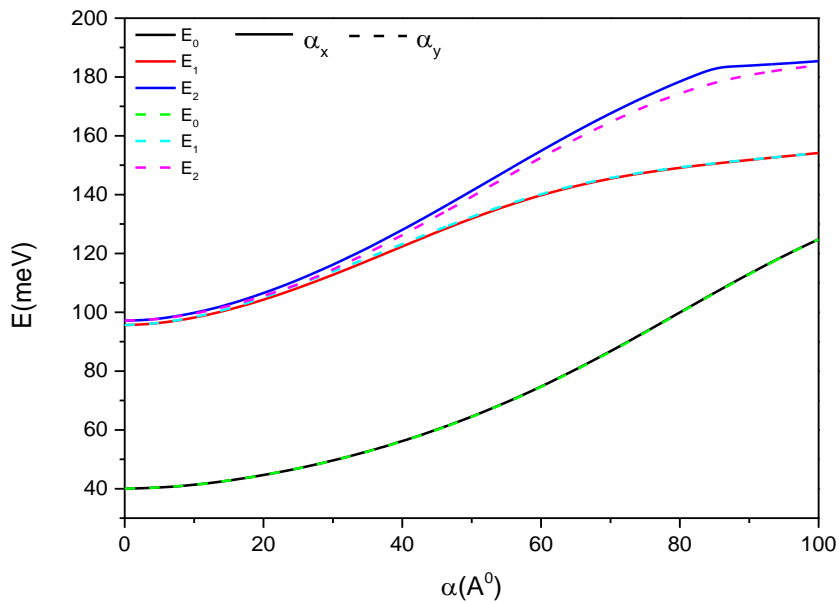

Figure3: Variation of the first three energy levels depending on the laser field applied in the x and y-directions
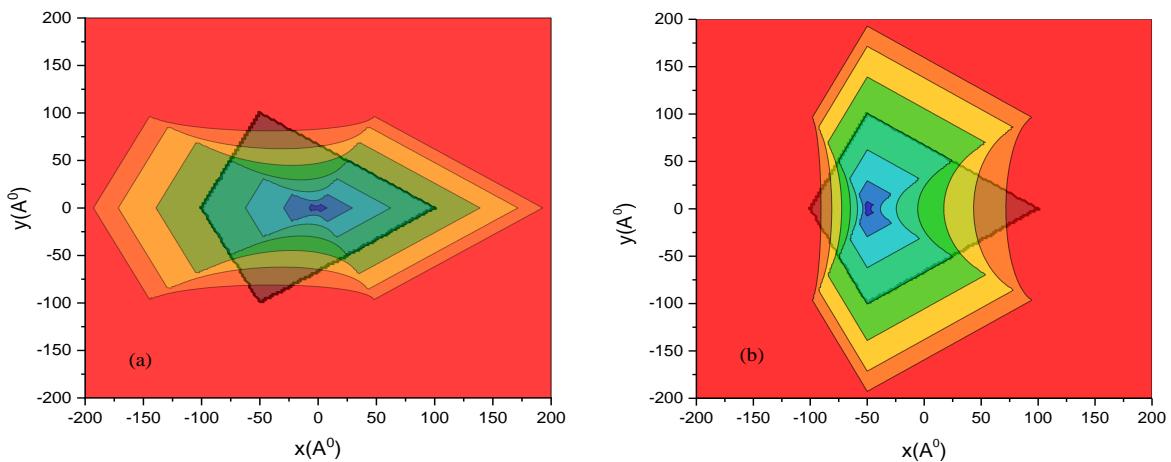

Figure4: Change in potential profile when laser light is applied ((a) when polarized laser light is applied in the x-direction, (b) when polarized laser light is applied in the x-direction)

16

Figure 5 shows the graph of 1st linear, 3rd degree nonlinear and total absorption coefficients. Although Figure 5(a) F=0-40 and 80 kV/cm was scanned, it was observed that the optical absorption coefficients of f=40 and 80kV/cm were zero. However, only F=40 kV/cm is shown on the graph. In Figure 5 (b), we applied an electric field of F=0-40 and 80kV/cm in the y- direction. contray to Figure 5 (a), it was observed that there was a decrease in absorption coefficients at F=40 and 80 kV/cm. All three absorptions correspond to the same photon energy range. In Figure 7, the refractive indexes of the same situation were calculated in (a) and (b). It was found to be in agreement with Figure 5.

Figure 5: Change of 1-2 optical absorption coefficients depending on the direction of the applied electric field; a) when applied in the x- direction b) when applied in the y- direction

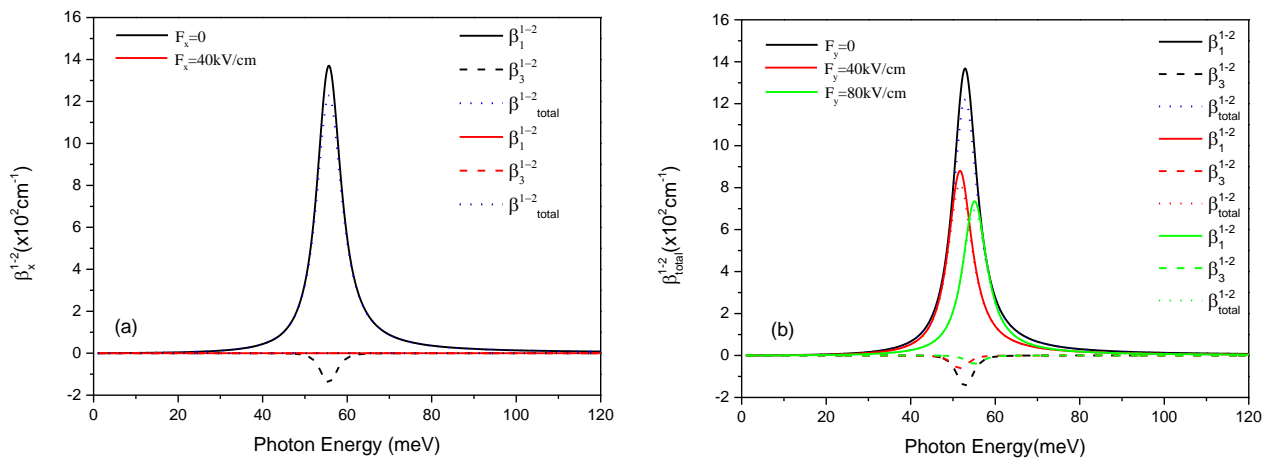**Figure6:** Change of 1-3 optical absorption coefficients depending on the direction of the applied electric field; a) when applied in the x- direction b) when applied in the y- direction

When we look at the optical absorption coefficients of 1-3 in Figure 6, only an absorption of F=0 is observed in the electric field applied in the x-direction, while there is no absorption at other values. However, when we apply an electric field in the y-direction again, it is observed that there is a decrease in the absorption coefficient and an increase in the required photon energy depending on the applied electric field strength. When we look at the reflection indices of the same situation (figure 8), as the electric field strength is increased, the refractive index decreases and the required photon energy increases.

Figure 7: Change of 1-2 optical refractive index depending on the direction of the applied electric field; a) when applied in the x- direction b) when applied in the y-direction
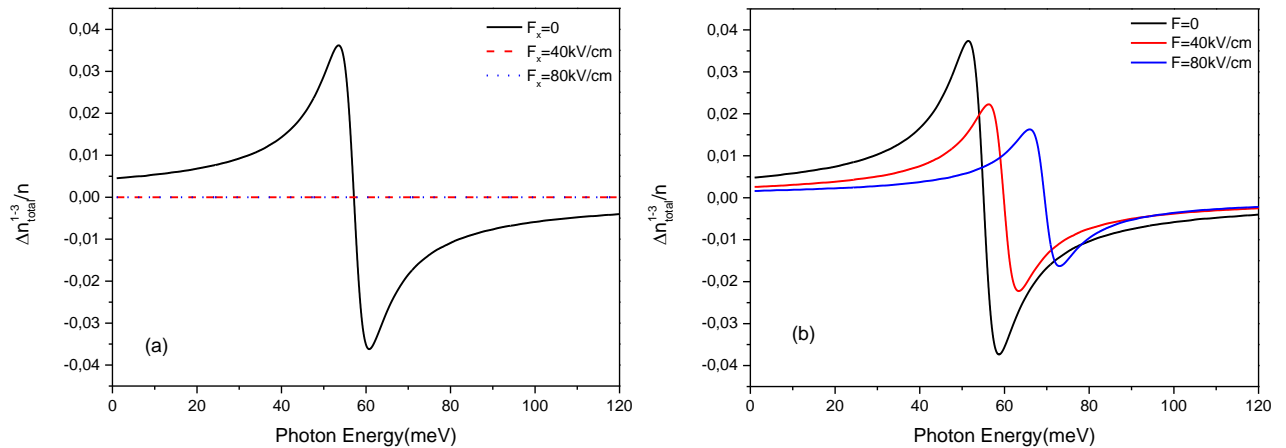
Figure8 : Change of 1-3 optical refractive index depending on the direction of the applied electric field; a) when applied in the x- direction b) when applied in the y-direction

18

In Figure 9, we applied intense laser light polarized in the x- direction (figure 9-(a)) and polarized in the y- direction (figure –(b)). When we applied the laser in the X-direction, there $\alpha = 40A^0$ was a shift to the left side, while there was a shift to the right side. The required photon energy has increased for $\alpha = 80A^0$. However, in Figure 9 (b), a polarized laser was applied in the y-direction. However, no absorption was observed other than its value $\alpha = 0$
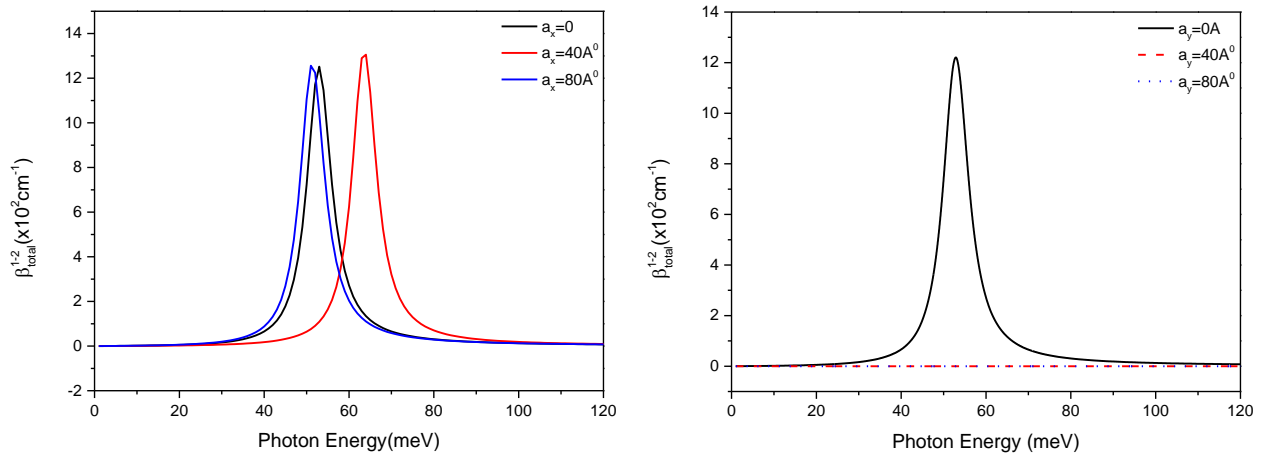
Figure 9: Change of 1-2 optical absorption coefficients depending on the direction of the applied laser field; a) when applied in the x- direction b) when applied in the y- direction
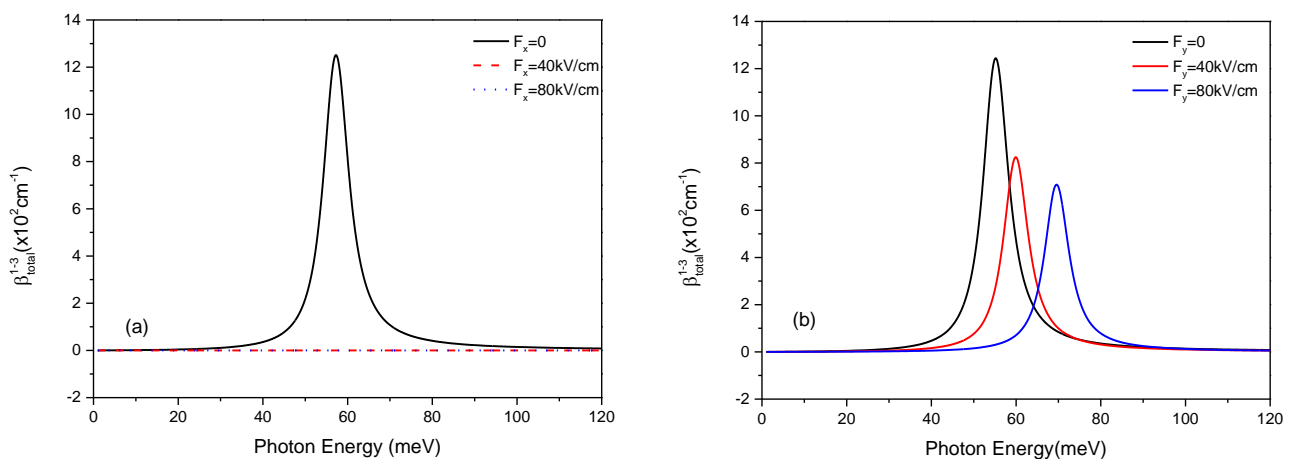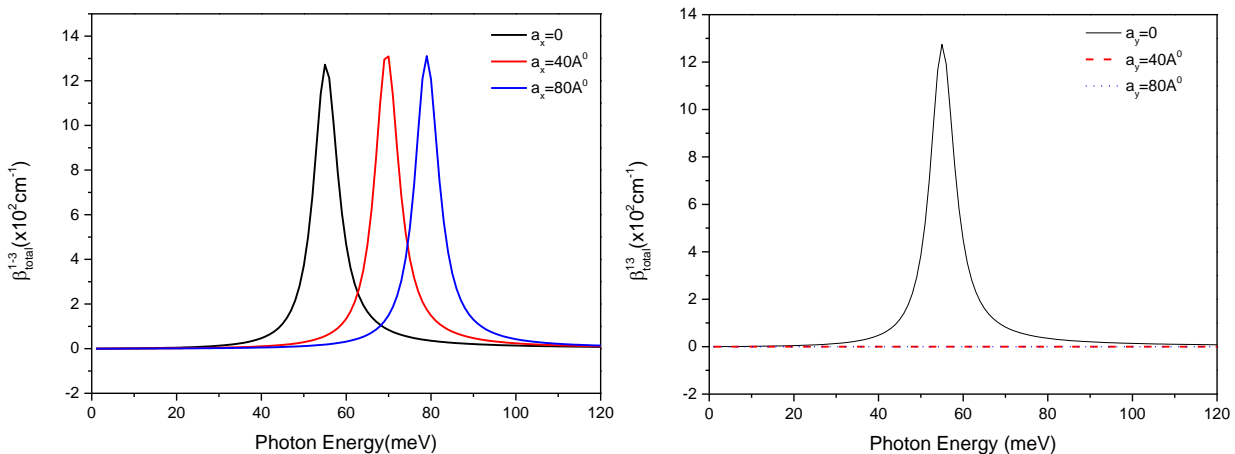

Figure10: Change of 1-3 optical absorption coefficients depending on the direction of the applied laser field; a) when applied in the x- direction b) when applied in the y-direction

19

Figure 10 is similar to figure 9. While there was no change in amplitude when intense laser light was applied in the x-direction, an increase in the required photon energy was observed as the laser intensity increased. Figures 11 and 12 show the reflection coefficients of figures 9 and 10, respectively, and it is seen that they are in agreement with these graphs.
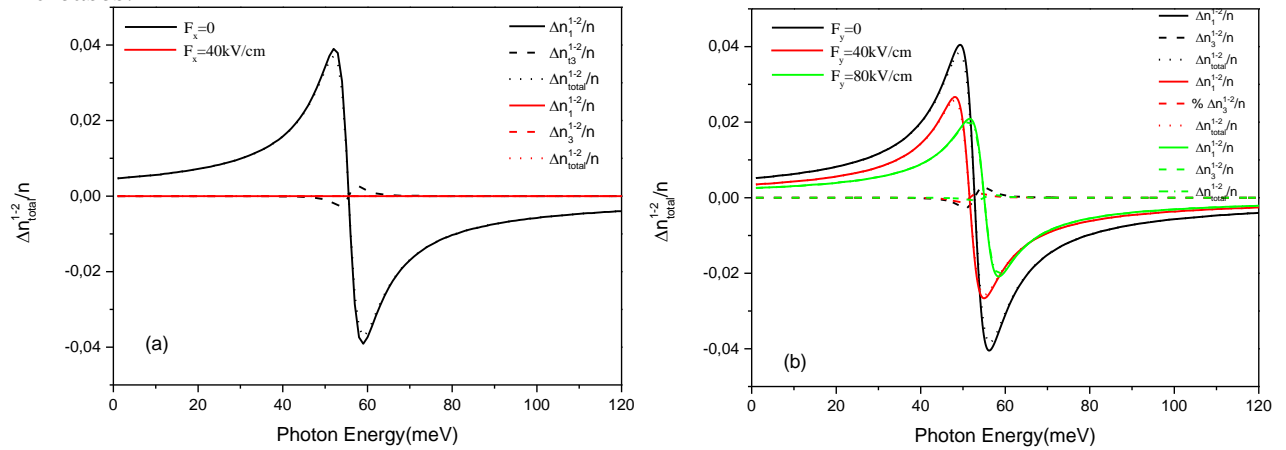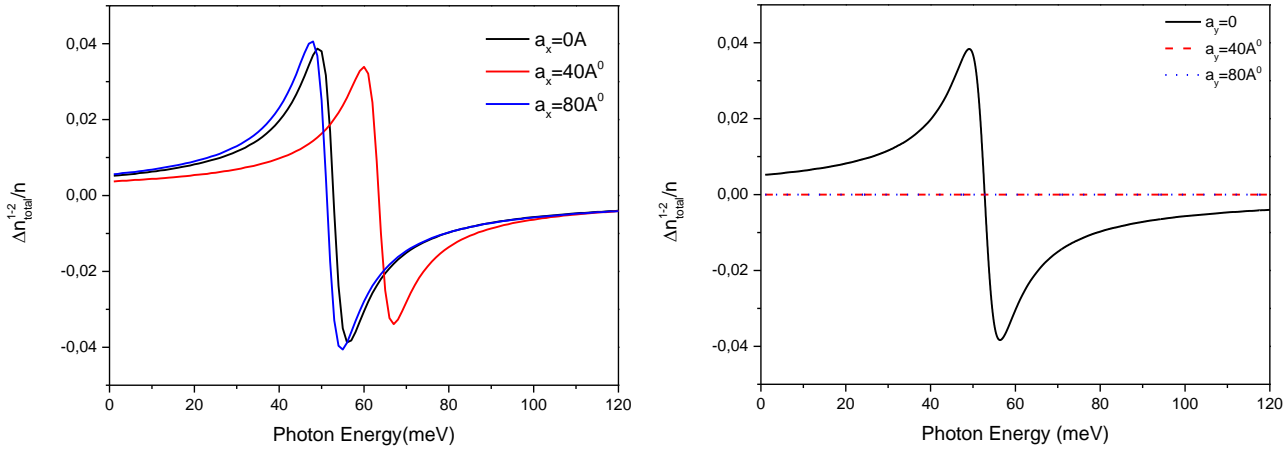

Figure 11: Change of 1-2 optical refractive index depending on the direction of the applied laser field; a) when applied in the x- direction b) when applied in the y- direction
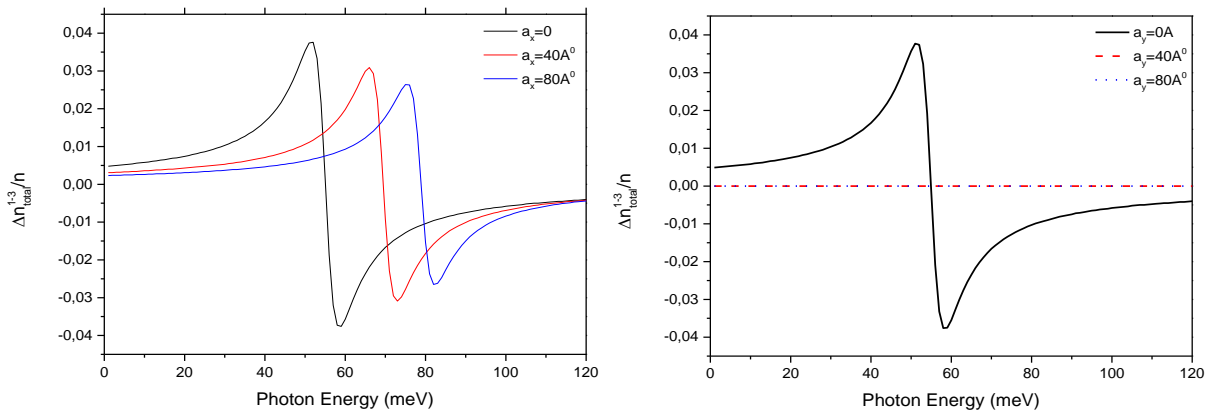
Figure12: Change of 1-3 optical refractive index depending on the direction of the applied laser field; a) when applied in the x- direction b) when applied in the y- direction

## 4. CONCLUSION

As a result, when an electric field is applied in arrowhead-shaped quantum wires, it is seen that the electric field applied in the y-direction changes these coefficients in 1-2 and 1-3 linear and nonlinear optical absorption transitions. When the laser field is applied, it is seen that when the x-direction polarized laser is sent, it has an effect on the absorption and refractive index. The effect of geometry and application direction on the system has been seen.

REFERENCES

[1]. Technology of Quantum Devices Manijeh Razeghi,springer l2010

[2]. MRS Bulletin , Volume 38 , Issue 9: Quantum dot light-emitting devices , September 2013 , pp. 685 – 691 DOI: https://doi.org/10.1557/mrs.2013.204

[3]. Shirasaki, Yasuhiro; Supran, Geoffrey J.; Bawendi, Moungi G.; Bulović, Vladimir . (2012). *Emergence of colloidal quantum-dot light-emitting technologies. Nature Photonics, 7(1), 13–23.* doi:10.1038/nphoton.2012.328

[4]. Fernando Sols, M. Macucci, U. Ravaioli, Karl Hess; Theory for a quantum modulated transistor. *J. Appl. Phys.* 15 October 1989; 66 (8): 3892–3906. https://doi.org/10.1063/1.344032

[5]. Fernando Sols, M. Macucci, U. Ravaioli, Karl Hess; On the possibility of transistor action based on quantum interference phenomena. *Appl. Phys. Lett.* 23 January 1989; 54 (4): 350–352. https://doi.org/10.1063/1.100966

[6]. J. Belhassen and A. Chelly, "Review of Selected Quantum Measurements Applied to Embedded Quantum Well in Nanoscale Transistor," in *IEEE Journal of Selected Topics in Quantum Electronics*, vol. 31, no. 5: Quantum Materials and Quantum Devices, pp. 1-8, Sept.-Oct. 2025, Art no. 1900108, doi: 10.1109/JSTQE.2024.3447163.

[7]. Thomas M. Mercier, Tasmiat Rahman, Chirenjeevi Krishnan, Edris Khorani, Peter J. Shaw, Michael E. Pollard, Stuart A. Boden, Pavlos G. Lagoudakis, Martin D.B. Charlton, High symmetry nano-photonic quasi-crystals providing novel light management in silicon solar cells, Nano Energy, Volume 84, 2021, 105874, ISSN 2211-2855, https://doi.org/10.1016/j.nanoen.2021.105874.

[8]. Gavin Conibeer, Martin Green, Richard Corkish, Young Cho, Eun-Chel Cho, Chu-Wei Jiang, Thipwan Fangsuwannarak, Edwin Pink, Yidan Huang, Tom Puzzer, Thorsten Trupke, Bryce Richards, Avi Shalav, Kuo-lung Lin, Silicon nanostructures for third generation photovoltaic solar cells, Thin Solid Films, Volumes 511–512, 2006, Pages 654-662, ISSN 0040-6090, https://doi.org/10.1016/j.tsf.2005.12.119.

[9]. A. Martí, N. López, E. Antolín, E. Cánovas, C. Stanley, C. Farmer, L. Cuadra, A. Luque, Novel semiconductor solar cell structures: The quantum dot intermediate band solar cell, Thin Solid Films, Volumes 511–512, 2006, Pages 638-644, ISSN 0040-6090, https://doi.org/10.1016/j.tsf.2005.12.122.

[10]. Kasapoglu, E. Non-resonant intense laser field and electric field effects on the optical characterization of Rosen-Morse quantum wells with different potential functions. *Opt Quant Electron* 56, 1425 (2024). https://doi.org/10.1007/s11082-024-07364-w

[10]. A. Shaer, M.B. Yücel, E. Kasapoglu, Hydrostatic pressure and temperature dependent optical properties of double inverse parabolic quantum well under the magnetic field, Physica B: Condensed Matter, Volume 685, 2024, 416057, ISSN 0921-4526, https://doi.org/10.1016/j.physb.2024.416057.

[12]. Kasapoglu, E., Yücel, M.B. & Duque, C.A. Electronic and optical properties of the exponential and hyperbolic Rosen–Morse types quantum wells under applied magnetic field. *Eur. Phys. J. Plus* **138**, 1026 (2023). https://doi.org/10.1140/epjp/s13360-023-04594-x

[13]. Kasapoglu, E.; Yücel, M.B.; Duque, C.A. Position-Dependent Effective Mass and Asymmetry Effects on the Electronic and Optical Properties of Quantum Wells with Improved Rosen–Morse Potential. *Condens. Matter* **2023**, *8*, 86. https://doi.org/10.3390/condmat8040086

[14]. E.C. Niculescu, L.M. Burileanu, A. Radu, Density of impurity states of shallow donors in a quantum well under intense laser field, Superlattices and Microstructures, Volume 44, Issue 2, 2008, Pages 173-182, ISSN 0749-6036, https://doi.org/10.1016/j.spmi.2008.03.005.

[15]. Vinasco, J.A., Radu, A., Niculescu, E. *et al.* Electronic states in GaAs-(Al,Ga)As eccentric quantum rings under nonresonant intense laser and magnetic fields. *Sci Rep* **9**, 1427 (2019). https://doi.org/10.1038/s41598-018-38114-0

[16]. G. Barseghyan, C.A. Duque, E.C. Niculescu, A. Radu, Intense laser field effects on the linear and nonlinear optical properties in a semiconductor quantum wire with triangle cross section, Superlattices and Microstructures, Volume 66, 2014, Pages 10-22, ISSN 0749-6036, https://doi.org/10.1016/j.spmi.2013.11.023.

[17]. I. Erdogan, O. Akankan, H. Akbas, Effects of hydrostatic pressure on the self-polarization in GaAs/Ga1−x Alx As quantum wells under the electric field, Physica E: Low-dimensional Systems and Nanostructures, Volume 42, Issue 2, 2009, Pages 136-140, ISSN 1386-9477, https://doi.org/10.1016/j.physe.2009.09.014.

[18]. Ozkapi, B., Mese, A.I., Cicek, E. and Erdogan, I. (2022), Self-Polarization of Hydrogenic Impurity in Quantum Wells Made of Different Materials. Phys. Status Solidi B, 259: 2200059. https://doi.org/10.1002/pssb.202200059

[19]. Sucu, S., Minez, S. & Erdogan, I. Self-polarization of a donor impurity for the first excited state in an Ga1-xAlxAs/GaAs quantum well. Indian J Phys 95, 1691–1695 (2021). https://doi.org/10.1007/s12648-020-01829-w

[20]. E. Cicek, A.I. Mese, B. Ozkapi, I. Erdogan, Combined effects of the hydrostatic pressure and temperature on the self-polarization in a finite quantum well under laser field, Superlattices and Microstructures, Volume 155, 2021, 106904, ISSN 0749-6036, https://doi.org/10.1016/j.spmi.2021.106904.

[21]. Akankan, O., Erdogan, I., Mese, A.I. et al. The effects of geometrical shape and impurity position on the self-polarization of a donor impurity in an infinite GaAs/AlAs tetragonal quantum dot. Indian J Phys 95, 1341–1344 (2021). https://doi.org/10.1007/s12648-020-01813-4

[22]. B. Bekar, F.K. Boz, S. Aktas, S. E Okan, The effect on the optical absorption coefficients due to the positions in the plane of square GaAs/Al(GaAs) quantum well wire under the laser field, Acta Phys. Pol., A, 136 (2019), pp. 882-888

A CFD STUDY ON HYDROGEN-ENRICHED METHANE COMBUSTION IN A TEST FURNACE

M.K. Büyükakın[1], O. Salcı[2], S. Öztuna[3]

[1,2,3]Mechanical Engineering Department, Faculty of Engineering, Trakya University, Edirne, TÜRKİYE

E-mail: mkbuyukakin@trakya.edu.tr

This paper examines a numerical investigation of hydrogen-enriched methane combustion in a test furnace at 60 kW thermal load. Fluent computational fluid dynamics (CFD) code was utilised for the numerical analysis. In the first part of the paper, the different combustion models, namely the partially premixed combustion and eddy dissipation model, were simulated for pure methane combustion cases. The air excess coefficient was taken as 1.2, 1.3 and 1.4, respectively. The calculated numerical results were compared with the experimental measurements. The results show that the NO_X emission level in the flue gas is calculated around 20% lower with the partially premixed combustion model, while it is calculated around 50% higher with eddy dissipation model. However, it is determined that both combustion model can perform the general variation trends in the experimental measurements. In the second part of the paper, the effects of hydrogen-enrichment of methane fuel on pollutants were investigated using eddy dissipation model, while keeping the thermal load constant at 60 kW. The hydrogen-enrichment was changed from 10% to 40% on molar base, respectively. The air excess coefficient was kept constant as 1.2 for all the cases. The obtained results show that the NO_X emission level in the flue gas does not change significantly up to 25% enrichment ratio, while it shows an increasing trend for enrichments above 25%.

Keywords: Methane combustion, Hydrogen-enrichment, NO_X emission

1. INTRODUCTION

Natural gas is the most commonly used fuel in the world both for domestic and industrial applications. It is mainly composed of methane with varying ratios of ethane, propane, butane and other molecules such as nitrogen and carbon dioxide. The methane ratio in natural gas is above 85% by volume and it could reach up to 97% depending on location of natural gas source. Although the majority of domestic and industrial applications heavily rely on natural gas, it is known that natural gas is a fossil fuel with a limited source on earth. Therefore, these systems have limited life time and the conversion of these conventional systems is inevitable in the near future.

Hydrogen is the best known fuel, which can replace fossil fuels in thermal energy systems. Hydrogen is not a fossil fuel, however, it can be produced from petroleum derived fuels and H_2O molecule. Although hydrogen fuel is not a renewable energy itself, the method applied to derive hydrogen molecule could be based on direct renewable energy systems such as solar energy systems. Hydrogen is considered as a clean fuel having no carbon atom and producing only H_2O in case it is reacted with oxygen. Hydrogen fuel has a higher heating value than natural gas or pure methane, which makes its flame temperature higher. This helps the considered boiler system have higher thermal efficiency accordingly. Thus, hydrogen fuel is favourable from the aspect of thermal efficiency and thermodynamics. However, in many cases, this result comes at the cost of increased NO_X formation rate, which is highly dependent on flame temperature. Therefore, the use of hydrogen as an alternative fuel needs careful investigation from the aspect of NO_X emissions. There are also other points such as increased laminar flame speed and flashback problems, which need to be considered, in case the hydrocarbon fuels are replaced with hydrogen. Consequently, hydrogen emerges as a carbon reducing, and efficient fuel, which needs further investigation and optimization both experimentally and numerically in terms of reducing NO_X pollutants. Some of the research studies on hydrogen-enriched combustion in the literature are reviewed. Odeh and Paul [1] numerically analysed the effect of hydrogen-enrichment of methane on flame characteristics. They determined that hydrogen-enrichment of methane fuel reduced CO_2 emissions, while the heat generation of combustion flame was reduced. Rajpara et. al [2] studied on the changing parameters of the combustion flame under the conditions of hydrogen-enriched methane combustion. It was concluded that the flame size turned into a shorter and wider size with hydrogen addition. Wang et. al [3] conducted experimental studies on metal fiber surfaces using hydrogen-enriched fuels. They studied two different modes of combustion and optimised operation conditions depending on flow velocity, laminar flame speed, jet diameter and the porosity of metal fiber. Schwarz et. al [4] studied experimentally on oxy-fuel combustion process of hydrogen-enriched methane between input power

of 100-140 kW. They determined that the increased hydrogen amount in the fuel increased the cooling capacity of the lances. Swaminathan et. al [5] numerically investigated the effects of hydrogen-enrichment of natural gas on NO_X pollutants in a furnace. Their results showed that, under the same heat input conditions, the NO_X emissions increased by 41.8% with hydrogen-enrichment ratio of 50% on molar base.

In this work, the effects of hydrogen-enrichment of methane fuel, up to 40% on molar base, on the flame parameters and pollutants in a test furnace, are numerically investigated with the use of Fluent code. The variation in the pollutant levels in the flue gas is determined depending on the enrichment ratio.

2. MATERIAL AND METHODS

2.1 Test Furnace and Mathematical Modelling

The solid model of the test furnace and the burner were modelled in SolidWorks software and their fluid volumes were created in Fluent Design Modeller. The solid models are given in Figure 1. The length and diameter of the furnace measures 1300 mm and 700 mm, respectively.
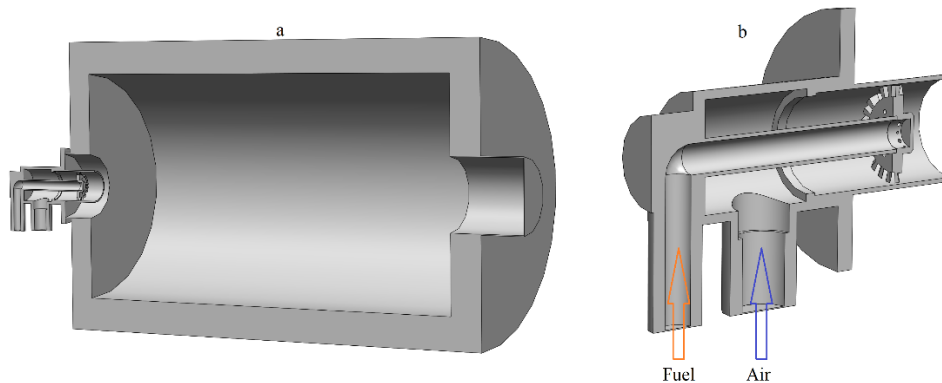
Figure 1 Solid Model of Furnace (a) and Burner (b)

The governing equations together with radiation intensity and chemical modelling equations were solved for the fluid volume of the furnace and burner under steady state conditions. The conservation of mass, momentum and energy equations, are given in Eqs. (1-3) [6-7].

$$\frac{\partial p}{\partial t} + \nabla.(\rho\mathbf{v}) = 0$$
(1)

$$\frac{Du_i}{Dt} = -\frac{\partial P}{\partial x_i} + \frac{\partial \sigma_{i\alpha}}{\partial x_\alpha} + \rho g_i$$
(2)

$$\frac{\partial(\rho h)}{\partial t} + \nabla.(p\mathbf{v}h) = \nabla.[\frac{k_t}{c_p}\nabla h] + S_h$$

(3)

In these equations, P is pressure, p is density, $\sigma_{i\alpha}$ is stress tensor, u is velocity, **v** is velocity vector**,** h is total enthalpy**,** k_t is thermal conductivty, c_p is specific heat and S_h is radiation source term. It is to be noted that these equations were solved by Favre-averaging in the turbulent flow. The radiation equation solved in this work is given in Eq. (4) [7].

$$\frac{d\,I(\vec{r},\vec{s})}{ds} + (\alpha + \sigma_s)\,I(\vec{r},\ \vec{s}) = \alpha n^2\frac{\sigma T^4}{\pi} + \frac{\sigma_s}{4\pi}\int_0^{4\pi} I(\vec{r},\vec{s}')\,\Phi(\vec{s},\vec{s}')\,d\Omega'$$

(4)

In Eq. (4), $\vec{r}$, $\vec{s}$, $\vec{s}'$, s, α , n, σ_s, σ, I, T, Φ and Ω' are position vector, direction vector, scattering direction vector, path length, absorption coefficient, refractive index, scattering coefficient, Stefan-Boltzmann constant (5.672 x 10^{-8} W/m²K⁴), total radiation intensity, local temperature (K), phase function and solid angle, respectively [7]. In addition, the chemical modelling equations were also solved for the numerical analysis. In this paper, two different models, namely the partially premixed combustion (PPC) model and eddy dissipation model (EDM), were taken in account. For PPC model, the mean mixture fraction ($\bar{f}$), the mean mixture fraction variance ($\overline{f'^2}$) and the mean progress variable ($\bar{c}$) were solved. These equations are given in Eqs. (5-7), respectively [7].

$$\frac{\partial(\rho\bar{f})}{\partial t} + \nabla.(\rho\mathbf{v}\bar{f}) = \nabla.(\frac{\mu_t}{\sigma_t}\nabla\bar{f})$$

(5)

$$\frac{\partial(\rho\overline{f'^2})}{\partial t} + \nabla.(\rho\mathbf{v}\overline{f'^2}) = \nabla.(\frac{\mu_t}{\sigma_t}\nabla\overline{f'^2}) + C_g\,\mu_t(\nabla\bar{f})^2 - C_d\,\rho\,\frac{\varepsilon}{k}\overline{f'^2}$$

(6)

$$\frac{\partial(\rho\bar{c})}{\partial t} + \nabla.(\rho\mathbf{v}\bar{c}) = \nabla.(\frac{\mu_t}{Sc_t}\nabla\bar{c}) + \rho S_c$$

(7)

Here in these equations, μ_t is turbulent viscosity, Sc_t turbulent Schmidt number and C_g, C_d and σ_t are model constants. In addition, k and ε are the turbulent kinetic energy and its dissipation rate, respectively. With the use of the flamelet modelling running on GRI-Mech 3.0 mechanism [8], which calculates the scalars like temperature and species mass fraction as a function of mixture fraction, the mean values of these scalars were calculated taking in account of the β- function PDF (probability density function) P(f) as;

$$\bar{\emptyset} = \bar{c}\int\emptyset_{burnt}(f)P(f)\,df + (1-\bar{c})\int\emptyset_{unburnt}(f)P(f)\,df$$

(8)

For EDM calculations, the transport equation for all the chemical species were solved individually as given in Eq.(9) and the reaction rate $\dot{\omega}_i$ was modelled as the sum of the reaction rates calculated in each reaction that i_{th} species participated.

$$\frac{\partial(\rho\overline{Y_j}))}{\partial t} + \nabla.(\rho\mathbf{v}\overline{Y_j}) = \nabla.(\frac{\mu_t}{Sc_t}\nabla\overline{Y_j}) + \overline{\dot{\omega}_i} \tag{9}$$

The reaction rate $R_{i,r}$ of i_{th} species in reaction r was modelled as the minimum of the Eq. (10) and Eq. (11) in Fluent Code [7]. Here, $\nu'_{i,r}$, $M_{\omega,i}$, A and B are stoichiometric constant, molecular weight and model constants.

$$R_{i,r} = \nu'_{i,r} \ M_{\omega,i} \ A \ \rho \ \frac{\epsilon}{k} \min \left(\frac{Y_R}{\nu'_{R,r} \ M_{\omega,R}} \right)$$

(10)

$$R_{i,r} = \nu'_{i,r} \ M_{\omega,i} \ A \ B \ \rho \ \frac{\epsilon}{k} \ \frac{\sum_P Y_P}{\sum_J^N \nu''_{j,r} M_{\omega,j}}$$

(11)

Two steps global reaction mechanism were taken in account for methane oxidation as given in Eq. (12);

$$CH_4 + 1.5 \ O_2 \longrightarrow CO + 2H_2O$$

$$CO + 0.5 \ O_2 \longrightarrow CO_2$$

(12)
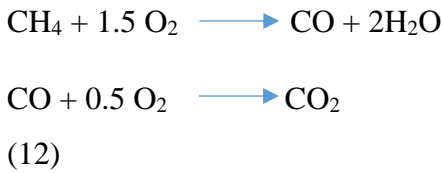
In case of hydrogen addition to methane, a third global reaction mechanism was added for hydrogen oxidation.

$$H_2 + 0.5 \ O_2 \longrightarrow H_2O$$

(13)
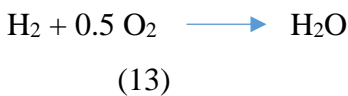
The NO_X emission calculations were run over the converged reacting flow field for both combustion models. Therefore, the NO_X emission transport equation, as given in Eq. (14), was solely solved over the converged solution.

$$\frac{\partial(\rho Y_{NO})}{\partial t} + \nabla.(\rho\mathbf{v}Y_{NO}) = \nabla.(\rho D\nabla Y_{NO}) + \dot{\omega}_{NO}$$

(14)

Thermal NO, prompt NO and N_2O route mechanisms were selected for NO_X formation [7]. For the turbulence modelling, standard k-ϵ was considered with default parameters in Fluent Code. The wall

temperature of the combustion chamber was set to 750K as thermal condition. The inlet temperature of fuel and air was taken as 288K. As for the numerical parameters, "Coupled" pressure-velocity coupling was set and second order upwind scheme was selected for the discretization of the equations, while PRESTO! was used for pressure. The scaled convergence criterion was 10^{-3} for all the equations, while it was 10^{-6} for energy, radiation intensity and NO_X emission equation. Polyhedral meshing elements were utilised for the reacting fluid volume. Around 2,800,000 elements were employed, which were determined from the cold flow analysis. The mesh elements above this number did not show considerable change in the axial velocity of the cold flow simulations in the centre of the furnace.

2.2 Validation of Mathematical Modelling

The simulations were run for PPC model and EDM employing 60 kW thermal power inlet of pure methane fuel. The air excess coefficient (λ) was adjusted as 1.2, 1.3 and 1.4 respectively. The obtained results, as the NO_X, CO_2 and O_2 emissions in the flue gas, and the flue gas temperature values were compared with the measurements supplied by ECOSTAR Company for natural gas combustion tests. Table 1 presents the comparison of the calculated molar emissions in the flue gas with the experimental measurements, together with the flue gas temperature comparison.

Table 1 Comparison of the Numerical Results and Measurements

Case	λ	CO_2 %	O_2 %	NO_X (PPM)	T_{flue_gas} (K)
PPC	1.2	9.56	3.24	40.85	942
EDM	1.2	9.56	3.25	71.26	1057
Experiment	1.2	9.5	3.49	50	878
PPC	1.3	8.71	4.54	36.59	915
EDM	1.3	8.66	4.62	72.66	996
Experiment	1.3	8.53	4.82	47	878
PPC	1.4	8.01	5.5	25.13	933
EDM	1.4	8.01	5.73	59.14	957
Experiment	1.4	8.28	5.94	37	863

The comparison given in Table 1 shows that both PPC and EDM models are able to simulate the general variation trends in the experimental measurements. The CO_2 and O_2 molar fractions are satisfactorily predicted by the two models, while the NO_X emission level in the flue gas and the flue gas temperature values are correctly predicted in terms of their variation trends and absolute levels, which are acceptable in the literature. It should be noted that the CO_2 and NO_X emissions are measured on dry-base and therefore, the numerical calculations are presented accordingly in Table 1.
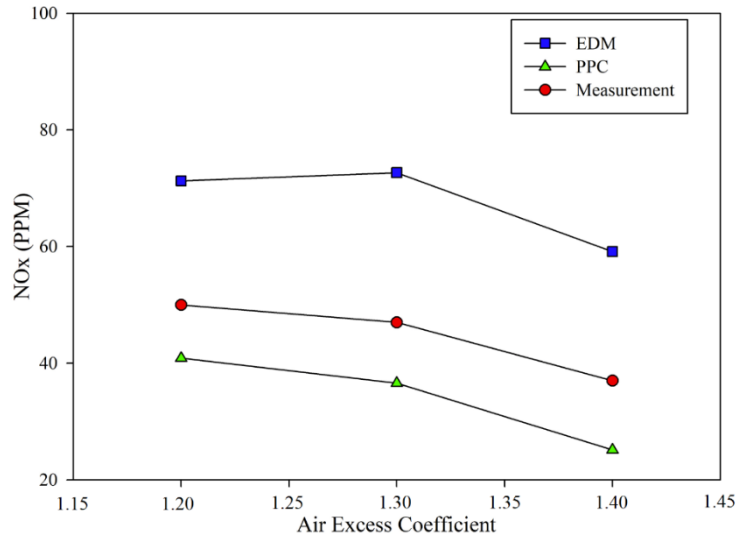
Figure 2 NO$_X$ Emission Variations

In addition, the compatible variation trend in the NO$_X$ emissions in the flue gas is also given in Figure 2.

3. RESULTS AND DISCUSSION

The effects of hydrogen-enrichment of pure methane fuel on combustion parameters and pollutants were simulated with the same numerical parameters. The air excess coefficient was 1.2 for all the cases. The hydrogen enrichment of pure methane was varied from 10% to 40% with 5% steps on molar base. For combustion modelling, EDM was employed for all the cases. In Table 2, fuel consumption and air flow rate variations according to the enrichment ratios are presented. The temperature variations calculated inside the furnace are illustrated in Figure 3.

Table 2 Fuel Consumption and Air Flow Variations

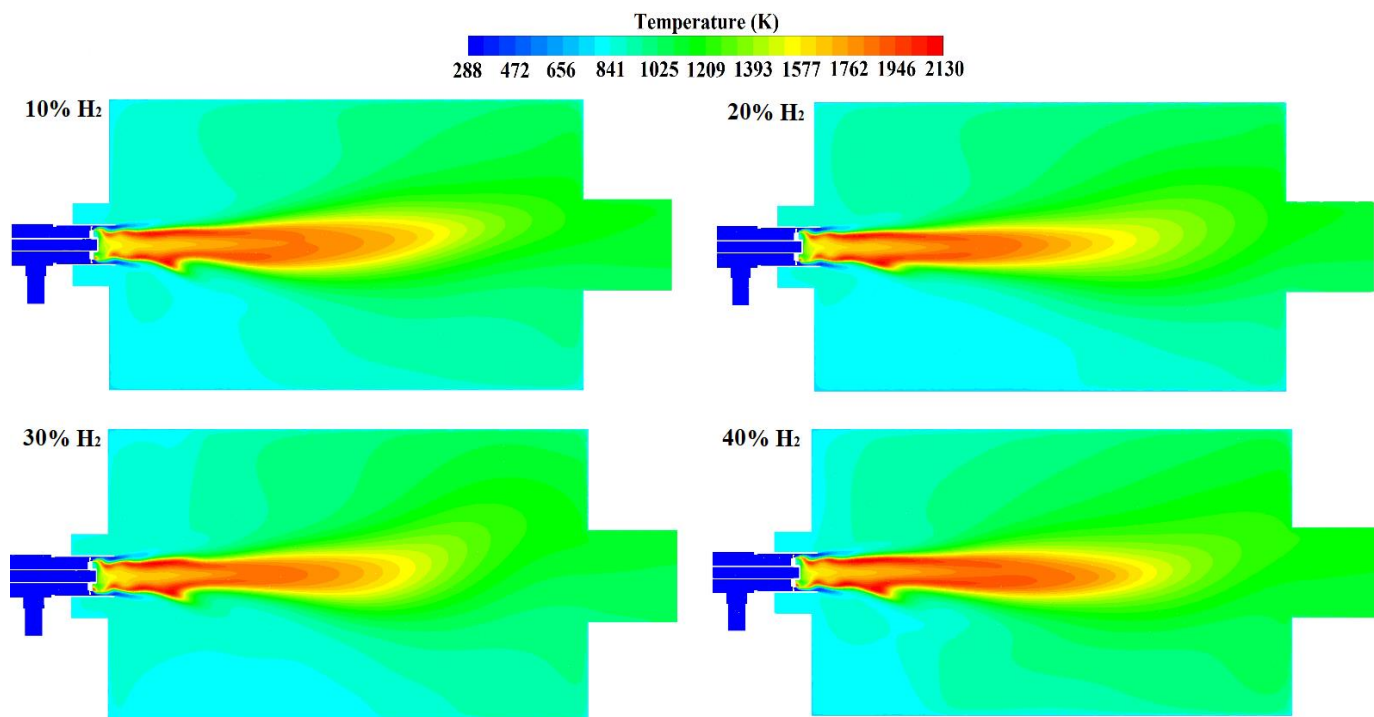| H$_2$ Enrichment % (Molar)	H$_2$ Enrichment % (Mass)	Fuel Consumption Rate (kg/s)	Air Flow Rate (kg/s)	Thermal Load (kW)
10	1.37	0.001177	0.024563	60
15	2.16	0.001164	0.024503	60
20	3.03	0.001151	0.024423	60
25	4	0.001136	0.024336	60
30	5.08	0.001120	0.024241	60
35	6.3	0.001102	0.024137	60
40	7.69	0.001083	0.024024	60

Figure 3 Temperature Variations in Furnace (xy plane)

It can be deduced from Figure 3 that the combustion flame shape and temperature do not show significant change with hydrogen addition. Although the hydrogen-enrichment ratio is up to 40% on molar base, this enrichment corresponds to 7.69% by mass, which does not cause considerable observable flame temperature change. However, a slight increase in the furnace temperature can be captured due to the higher heating value of hydrogen fuel compared to methane fuel. Table 3 presents the calculated molar CO_2, O_2 and NO_X emissions in the flue gas counting in the water content of the flue gas.

Table 3 Calculated Emissions in Flue Gas

H_2 Enrichment % (Molar)	CO_2 %	O_2 %	NO_X, (PPM)
0	8.01	3.24	58
10	7.79	3.24	56
15	7.77	3.14	58
20	7.5	3.17	64
25	7.3	3.3	65
30	7.2	3.1	73
35	7.04	3.15	85
40	6.8	3.2	103

It should be noted that the water content in the flue gas does not significantly change up to 40% of hydrogen enrichment. Table 3 shows that hydrogen-enrichment gradually decreases the molar

fraction of CO_2 in the flue gas. This is mainly due to the fact that hydrogen fuel does not contain carbon atom. The slightly increasing water content in the flue gas, together with the increasing O_2 molecule in the air per CH_4 molecule in the fuel is another factor reducing the CO_2 molar fraction in the flue gas. From this aspect, hydrogen can be considered as a clean fuel as expected. The calculated results show that the NO_X emissions in the flue gas show an increasing trend with the increasing enrichment ratio. This occurs due to the higher flame temperature values obtained with the hydrogen-enrichment. However, the calculated results show that the increase in the NO_X emissions is quite acceptable up to the enrichment ratio of 25% on molar base. This result is most likely due to the very low mass fraction of hydrogen in the fuel mixture, which supresses the flame temperature and the formation of thermal NO up to a certain point of enrichment. This enrichment point is determined to be 25% in this study. Above this enrichment ratio, hydrogen fuel acts as a pollutant fuel from the NO_X emissions aspect. It is known from the available literature that the NO_X emissions are mainly formed through the thermal route for hydrocarbon fuels and hydrogen, which is highly effective for temperature levels above 1800K. Therefore, the temperature variations are shown in Figure 4 in a restricted scale given from the minimum value of 1800K to a maximum calculated value of 2130K. Figure 4 proves that although the general flame shape remains similar and the maximum flame temperature is also calculated very close to each other, the fluid volume having temperature above 1800K is expanded with the increasing hydrogen-enrichment ratio, especially beyond 30% enrichment on molar base, which explains the NO_X emission variations in Table 3. The higher heating value of hydrogen fuel and its low density are the main underlying physical effects on this behaviour of the NO_X emissions.
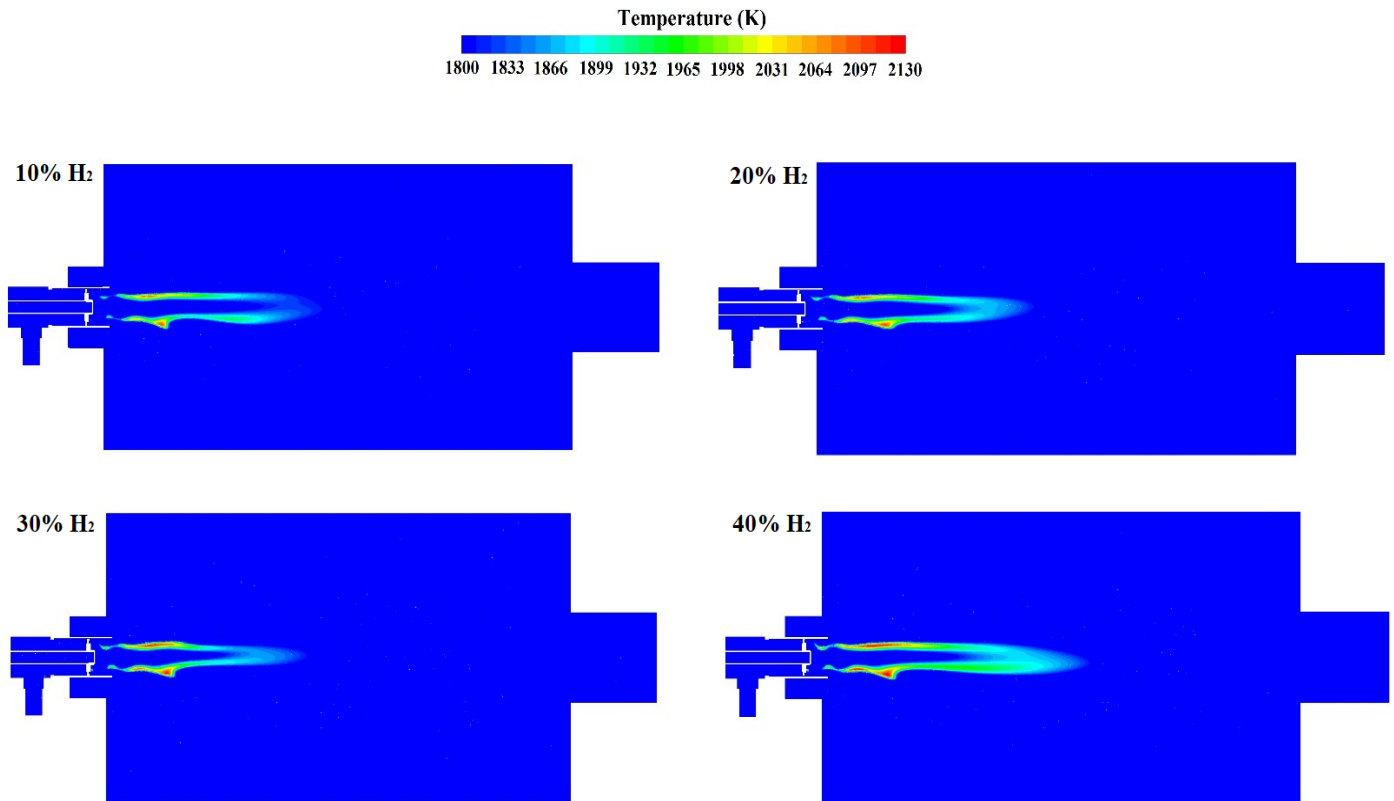
Figure 4 Temperature Variations in Furnace in a Restricted Scale (xy plane)

4. CONCLUSION

In this study, two different combustion models were utilised for the numerical simulations and the validation of these combustion models were obtained for methane combustion cases. Then, the effects of hydrogen-enrichment of methane fuel, employing EDM combustion model, on the pollutants and the flame parameters were numerically investigated. The following results can be achieved from this study;

- The hydrogen-enrichment does not affect the general flame shape up to 40% enrichment ratio on molar base.

- Hydrogen fuel can be assumed as a clean fuel for not having carbon atom and reducing CO_2 emissions.

- The hydrogen-enrichment of methane fuel increases the local flame temperature, which tends to increase the NO_X formation rate.

- The hydrogen-enrichment does not significantly increase the NO_X emissions in the flue gas up to the enrichment ratio of 25%. Above this enrichment ratio, hydrogen fuel can be considered as a pollutant fuel from the aspect of NO_X emissions and needs careful investigation accordingly.

REFERENCES

[1] Odeh, A., Paul, M.C., Effects of hydrogen enrichment on the heat generation and emission of natural gas turbulent premixed flame, International Journal of Hydrogen Energy, 49, 1176-1191, 2024

[2] Rajpara, P., Shah, R., Banarjee, J., Effect of hydrogen addition on combustion and emission characteristics of methane fuelled upward swirl can combustor, International Journal of Hydrogen Energy, 43, 17505-17519, 2018

[3] Wang, T., Zhang, Y., Zhang, H., Lyu, J., Stability and emissions of hydrogen-enriched methane flames on metal fiber surface burners, International Journal of Hydrogen Energy, 72, 1308-1320, 2024

[4] Schwarz, S., Daurer, G., Gaber, C., Demuth, M., Priler, R., Hochenauer, C., Experimental investigation of the combustion characteristics in oxy-fuel combustion of hydrogen-enriched natural gas on a semi industrial scale, International Journal of Hydrogen Energy, 49, 323-337, 2024

[5] Swaminathan, S., Spijker, C., Raonic, Z., Koller, M., Kofler, I., Raupenstrauch, H., Numerical study of an industrial burner to optimise NOx emissions and to evaluate the feasibility of hydrogen-enriched fuel, International Journal of Hydrogen Energy, 49, 1210-1220, 2024

[6] Law, C.K., Combustion physics, Cambridge University Press, 2006

[7] ANSYS Fluent theory guide. 2021. https://dl.cfdexperts.net/cfd_resources/Ansys_Documentation/Fluent/Ansys_Fluent_Theory_Guide.pdf. Accessed 30 June 2024

[8] Smith GP, Golden DM, Frenklach M, Moriarty NW, Eiteneer B, Goldenberg M, Bowman CT, Hanson RK, Song S, Gardiner WC, Jr, Lissianski VV, Qin Z. http://www.me.berkeley.edu/gri_mech/. Accessed 30 June 2024

ENERGY PERFORMANCE SIMULATION AND MODEL CALIBRATION OF A BUILDING USING IN-SITU ENERGY USE DATA

K. Rezaie[1], M. Özdenefe[1,2]

[1]*Department of Mechanical Engineering, Faculty of Engineering, Eastern Mediterranean University, Famagusta, North Cyprus via Mersin 10, TÜRKİYE*
[2]*Energy Research Centre, Eastern Mediterranean University, Famagusta, North Cyprus via Mersin 10, TÜRKİYE*

E-mail: 22500963@emu.edu.tr
murat.ozdenefe@emu.edu.tr

This work is an effort to develop an energy model and carry out an energy performance simulation of a selected building as well as to calibrate the energy model by employing in-situ energy use data. The work strives to provide a basis for effective decision-making for possible energy conservation measures and optimization studies. The selected building is the Health Centre Building located in the Eastern Mediterranean University Campus, at Famagusta, North Cyprus. Design Builder software is employed for developing an energy model and carrying out performance simulation. One year (August 2022-July 2023) in-situ electricity use data of the building is retrieved and employed for the energy model calibration. Calibration will be performed by comparing the simulation results with the real measured in-situ electricity use and reconciling the two via iterative tuning of the major parameters: U-values of the building fabric, efficiencies/COPs of AC unites, internal heat gains, and schedules of various operations. In-situ measurements of certain parameters such as U-values of the walls and ceiling, indoor air temperature and relative humidity were also performed and the relevant parameters will be inputted to the energy model to further enhance the prediction accuracy of the energy model. The preliminary energy model of the building was generated and successful energy performance simulations were performed. It has been found that the model predicted the annual electricity use as 75459.3 kWh which is 6.6% less than the in-situ/actual electricity use of 80815.0 kWh. Although the discrepancy between the annual simulated and actual electricity use seems moderate, monthly CV(RMSE) and NMBE values were found to be 54.1% and 7.2% respectively which do not satisfy the ASHRAE standard (CV(RMSE) =15% and NMBE =5% respectively) for the calibrated model. In the subsequent phases of this work, tuning of the aforementioned parameters will be done and a series of simulations will be performed to attain the acceptable error for satisfying the ASHRAE standard.

Keywords: Building energy model development, Energy performance simulation, Calibration, In-situ energy monitoring

1. INTRODUCTION

Energy use in buildings accounts roughly half of the total energy use of the world. This allows us to consider energy efficiency in the context of buildings as a vast source of unexploited clean energy which can be tapped by smart design options. This indeed requires building energy modelling and simulation for swift appraising of the design decisions. Since it provides information about a building's energy-use profile, energy modelling and simulation is essential for helping stakeholders to decide which energy-saving initiatives to implement. Accurate energy models can cause a drastic reduction in energy use and operational costs by finding and remedying inefficiencies within building systems. In order to achieve this energy models of the buildings should be calibrated using real, in-situ energy use data. Model calibration paves the way for accurate estimation of real energy use which requires validation of the simulation results by comparing and reconciling with the actual energy use data. This process increases the reliability of the energy models [1].

Recently, plenty of research about the of energy performance simulation and calibration for enhancing building energy efficiency has been done. For instance, Swan and Ugursal offer the detailed overview of building energy use and working on two modelling approaches, bottom-up and top-down. In this research they found that top-down approach is useful for general benchmarking, on the other hand bottom-up is important method for detailed simulation that can improve the energy-saving strategies in buildings [2]. To support this, Kavgic et al. explain more about the bottom-up modelling approach methodologies, for more accuracy, it uses micro-level data aggregation at the urban scale[3]. Reinhart and Cerezo Davila add to this research by emphasizing the three primary stages of urban energy modelling: data input, thermal modelling, and validation. They reach the point that proper calibration is needed for more accuracy and reliability of the energy predictions made by simulation tools. In actual use, statistical regression and machine learning methods have a significant effect on improving the results of the calibration process, as highlighted in Cerezo Davila et al. and Sola et al. In actual use, statistical regression and machine learning methods have a significant effect on improving the results of the calibration process, as highlighted in Cerezo Davila et al. and Sola et al., whose research area is about the calibration and validation of building energy models at the urban scale[4] [5]. Furthermore, Li et al. discuss the updated review of modelling approach and highlighting the need for continuous development in calibration techniques to be compatible with the dynamic nature of urban environments and their energy demands [6]. A substantial review by Frayssinet et al. argue different calibration techniques and their impact on the accuracy of energy simulation, offering the ongoing refinement in these methods is critical to improving model predictions and optimizing energy use in real-world settings[7].

In this work an energy model of a selected building is developed, and energy performance simulation is performed. One-year actual electricity consumption of the building is also retrieved and is used for calibrating the model. The work intends to provide a basis for effective decision-making for possible energy conservation measures and optimization studies. The selected building is the Health Centre on the campus of the Eastern Mediterranean University in Famagusta, North Cyprus. The Design Builder software was utilized in order to develop an energy model and conduct its performance simulations. One year of in-situ electricity consumption data was employed for calibration of the energy model between August 2022 and July 2023. The calibration process required the comparison between the results from the simulation and the actual measured use of electricity, affinity by iteratively adjusting some of the main parameters: U-values of the building fabric, internal heat gains, and operational schedules. Moreover, various in-situ measurements have been done, like U-values of the walls and ceiling, indoor air temperature, and relative humidity. For more accuracy and reliability this information is utilized in the energy model.

2. MATERIAL AND METHODS

The building is modelled and simulated with Design Builder software. The output is then compared with actual data from hourly electricity meter, and the difference between the two must be reduced until it satisfies the ASHRAE standard's requirements for Mean Bias Error (MBE) and Coefficient of Variation of the Root Mean Square Error CV (RMSE), which are 5% and 15%, respectively.

2.1 Building Information and Energy Data Collection

The Health Center building at Eastern Mediterranean University includes two floors, and the area of the ground and first floors is 451.5 and 804.5 m^2, respectively. The building is oriented in an east-west direction to receive more light during the day in areas of patient care, and at the same time, for the windows in this direction, shadings are used to reduce the excessive summer heat gain through windows.

Figure 1: The Health Centre building at Eastern Mediterranean University

External walls are perforated brick with inner and outer cement plaster layers, and the roof is reinforced concrete. All windows are with double-glazing and PVC frames. The first floor comprises from 18 rooms while the ground floor 13 rooms. Figure 2 and Figure 3 illustrate the room layout and distribution in the first and ground floor.
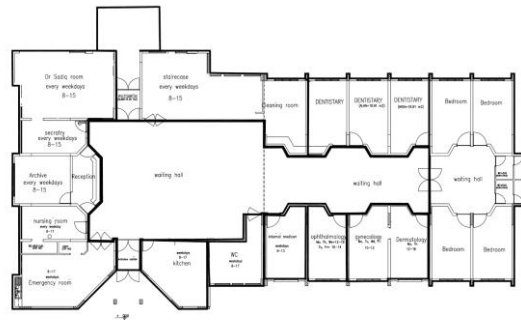

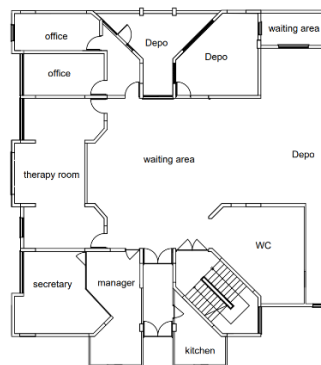**Figure 2**: First floor room layout and distribution

Figure 3: Ground floor room layout and distribution

Each room is equipped with individual split unit air conditioning systems, fully capable of providing heating and cooling. There is no central HVAC system for the building

2.2 Energy Modelling and Simulation

Design Builder software was used to construct an energy model of the Health Center building, considering all of the static and dynamic variables relevant for North Cyprus. This model was created to provide an as-built representation of the structure using architectural drawings and measured data. The input data consisted of thermophysical properties of building components, internal heat gains, and schedules related to a variety of operational periods for different rooms. All the climatic data in an hourly basis for temperature, humidity, and solar radiation were downloaded from the online climate data repository and imported into the Design Builder software for simulation purposes [8]. Figures below show the zoning of the first and ground floor of the building. Every zone has been labelled regarding its function; therefore, the simulation will consider different energy needs for each space.
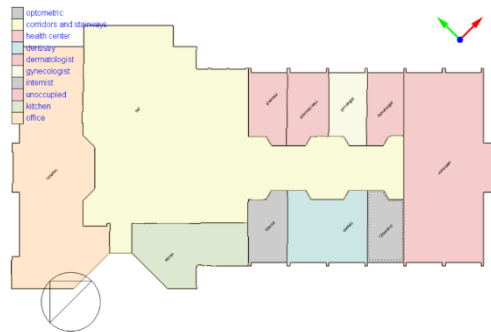

Figure 4: Zoning of the First Floor in the Health Center, depicting various functional spaces such as dentistry, dermatology, gynaecology, internal medicine, and unoccupied areas.
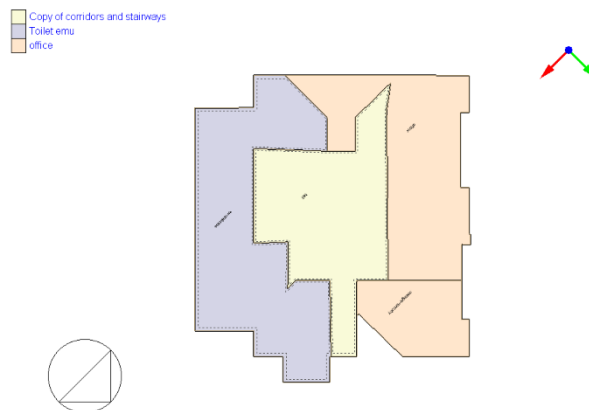

Figure 5: Zoning of the Ground Floor in the Health Center, including corridors, stairways, office spaces, and toilets.

Obtaining the local climatic data was quite relevant for the simulation of the building under study to be as close to a real consumption scenario as possible. The electricity usage data, which

covered the period August 2022 to July 2023, was gathered from the university's energy management system and utilized for model calibration.

2.2.1 Building Envelope

The thermal properties of the building's internal and external walls, floors, and ceiling were crucial to the energy model. Detailed information regarding these components is presented in Table 1, Table 2, Table 3, and Table 4.

Table 1 Internal walls composition and thermal properties[9], [10]

Layers	Material	Thickness (mm)	k-value (W/m.K)	Specific heat transfer (kJ/kg. K)	Density (K/m^3)
1	Plastic paint	0.5	0.5	4800	900
2	Satin plaster	12	0.35	1149	640
3	Plaster	25	0.5	1000	1300
4	Perforated Clay Brick	20	1.31	800'000	1700
5	Plaster	25	0.5	1000	1300
6	satin plaster	12	0.35	1149	640
7	Plastic paint	0.5	0.5	4800	900

Table 2. External walls composition and thermal properties[9], [10]

Layers	Material	Thickness (mm)	k-value (W/m.K)	Specific heat transfer (kJ/kg. K)	Density (K/m^3)
1	Plastic paint	0.5	0.5	4.8	900
2	Plaster	25	0.5	1	1300
3	Perforated Clay Brick	20	1.31	800	1700
4	Plaster	25	0.5	1	1300
5	Plastic paint	0.5	0.5	4.8	900

Table 3. Exterior floor composition and thermal properties[9], [10]

Layers	Material	Thickness (mm)	k-value (W/m.K)	Specific heat transfer (kJ/kg. K)	Density (K/m^3)
1	Mosaic	40	2.38	0.94	2500
2	Mortar	30	0.8	0.8	1800
3	Sand	30	0.8	1.2	1800
4	concrete	100	2.5	1	2500
5	concrete blocks	150	1.5	1	2400

Table 4. Iinterior floor composition and thermal properties[9], [10]

Layers	Material	Thickness (mm)	k-value (W/m.K)	Specific heat transfer (kJ/kg. K)	Density (K/m^3)
1	Water insulation based on bitumen	4	0.5	1.25	1500
2	Levelling concrete	50	0.5	1050	2500
3	Reinforced concrete	150	0.5	1050	2500

2.2.2 U-Value Measurement

Collected data from direct measurements and utility data were used to represent correctly the energy performance of the building. A special kit was mounted in place to measure the U-value of walls and ceiling during the hottest weeks of summer to ensure the energy model really captures the actual thermal performance of the building. Besides, temperature sensors were installed to record indoor environmental conditions, thus providing useful data required to enhance the accuracy of the energy model [11]. The sensors were fixed on the external wall, out of the windows for a sufficient distance not to be influenced by the surrounding elements. They used an exterior temperature probe to detect the background conditions and inside sensors to record temperature variations at the walls and ceiling. The data acquisition process was done over a period of 1.5 to 2 hours to achieve stabilized U-value fluctuations.

Figure 6: Experimental setup for U-value measurement of the ceiling using external sensors.

These U-value measurements were used to provide input to the energy model in an attempt to better the calibration of the model, showcasing a more representative and closer-to-actual thermal performance of the building envelope. The wall U-value measured 2.364 W/m²K, and that for the ceiling was 5.418 W/m²K. These values will then be used to ensure that the energy model reflects actual thermal characteristics. Figures 7 and 8 illustrate the U-value fluctuations of the wall and ceiling, respectively, measured during this period.
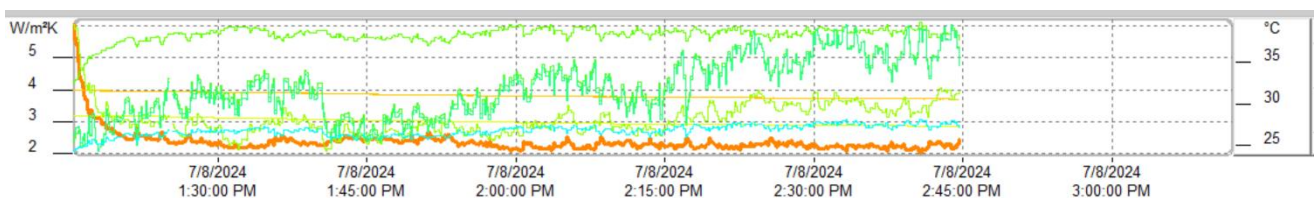

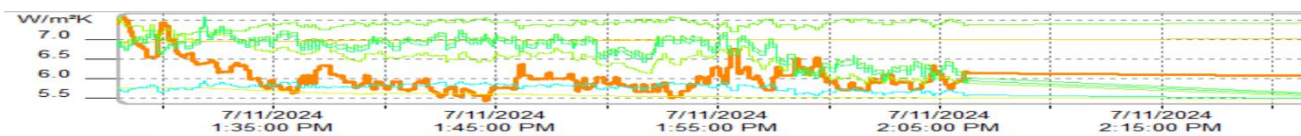**Figure 7**: U-value fluctuations of the wall measured on the hottest Day

Figure 8: U-value fluctuations of the wall measured on the hottest Day

42

2.2.3 Operational Schedules

The operating schedules below have been developed in an attempt to simulate the real energy use profiles of the Health Center by modelling hours of occupancy and usage for the various areas. In fact, the schedules form part of the major input that determines when the systems (like AC units), lighting, and internal gains or equipment (like computers) and occupant-related heat gains are on. It is then assumed that AC units run only during occupancy hours in every room, meaning heating or cooling can be given out if the space is occupied. Similarly, it is assumed that lighting and other electrical equipment remain on when these hours are operational. Otherwise, the AC units and lights are kept turned off to minimize the usage of energy when rooms are unoccupied.

Tables 7 and 8 are operating schedules for the first and ground floors, respectively. These give an approximation as to what time of every week each space is being used. This operating schedule will be able to allow the simulation to more accurately model real energy use by aligning the operation of AC units, lighting, and other equipment with real world usage patterns.

Table 5. First floor schedules

Service	Monday	Tuesday	Wednesday	Thursday	Friday
Ear-nose-throat	8:00-12:00, 13:00-17:00	8:00-12:00, 13:00-17:00	8:00-12:00, 13:00-17:00	8:00-12:00, 13:00-17:00	8:00-12:00, 13:00-17:00
Ophthalmology	12:00-16:00	10:00-14:00	12:00-16:00	12:00-16:00	10:00-14:00
Dermatology	12:00-16:00	-	12:00-16:00	-	-
Dentist	9:00-13:00	9:00-13:00	9:00-13:00	9:00-13:00	9:00-13:00
Internal Medicine	9:00-13:00	9:00-13:00	9:00-13:00	9:00-13:00	9:00-13:00
Gynaecology	10:00-12:00	10:00-12:00	10:00-12:00	-	10:00-12:00
Kitchen	8:00-17:00	8:00-17:00	8:00-17:00	8:00-17:00	8:00-17:00
Reception	8:00-17:00	8:00-17:00	8:00-17:00	8:00-17:00	8:00-17:00
Manager Office	8:00-17:00	8:00-17:00	8:00-17:00	8:00-17:00	8:00-17:00
Nursing Room	8:00-17:00	8:00-17:00	8:00-17:00	8:00-17:00	8:00-17:00
Emergency Room	8:00-17:00	8:00-17:00	8:00-17:00	8:00-17:00	8:00-17:00

Table 6. Ground floor schedules

Service	Monday	Tuesday	Wednesday	Thursday	Friday
Manager Office	8:00-17:00	8:00-17:00	8:00-17:00	8:00-17:00	8:00-17:00
Secretary Office	8:00-17:00	8:00-17:00	8:00-17:00	8:00-17:00	8:00-17:00
Kitchen	8:00-17:00	8:00-17:00	8:00-17:00	8:00-17:00	8:00-17:00
Research Office	8:00-17:00	-	8:00-17:00	-	-
Hall	8:00-17:00	8:00-17:00	8:00-17:00	8:00-17:00	8:00-17:00
Assistant Office	8:00-17:00	8:00-17:00	8:00-17:00	8:00-17:00	8:00-17:00
Depository	-	-	-	-	-

2.3 Calibration Process

One year of in-situ electricity usages data were used to perform the energy model calibration. Calibration's main goal is to reduce differences between measured real data and simulation data. The model should be representative of actual energy consumption by the building. Efficiencies of HVAC systems are not a concern in model calibration; this is still under investigation. A good agreement between the preliminary comparison of the simulated and real data of electricity consumption has been performed, meaning that the energy model behaves similarly to the real performance of the building.

Two of the most important statistical indicators recommended for the calibration process by ASHRAE were used: Coefficient of Variation of the Root Mean Square Error, CV(RMSE), and Mean Bias Error (MBE).

The CV(RMSE) calculates the variance between the model results and actual data; the lower the value, the better the model is fitted to the observed data. The MBE gives the overall systemic bias of the model through the differences between the simulated and observed energy usage for every hour of the study period. Being in a percentage form, it will clearly show the bias of the model. The current model calibration is yielding around 7.2% in MBE and 54.1% in CV(RMSE) for the monthly data series at this stage. All these point to a reasonable representation the model has with respect to energy use at the building, though further refinement is required for better accuracy. Note that results are preliminary, and model parameters are continually being updated to increase the accuracy of the model[12].

3. RESULTS AND DISCUSSIO

The recorded and simulated electricity consumption of the health center for the period between August 2022 and July 2023 is visualized above. The recorded data in this graph denotes actual monthly electricity consumption by the facility, while the simulated data derives from energy modeling. This supports an effective review of the simulation accuracy by underlining gaps between

predicted and actual consumption, therefore leading to further adjustments of models for future alignment in performance.
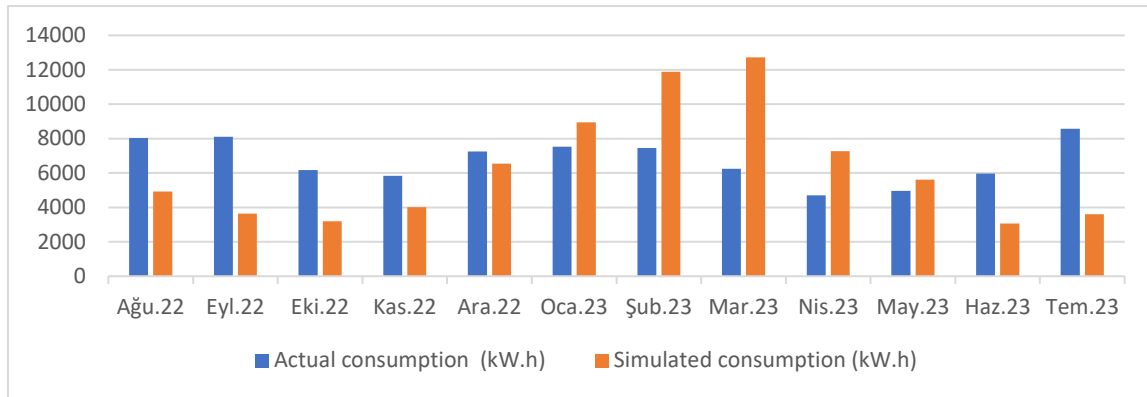

Figure 9: Actual vs. simulated monthly electricity consumption (kWh) for the health center (Aug 2022 - Jul 2023).

2.1 Calibration Insights

The energy model calibration is still in the process, but a considerable difference between real and simulated data can be noticed. Two key performance indicators relied on for the purpose of validation are: Coefficient of Variation of the Root Mean Square Error (CV(RMSE)) and Normalized Mean Bias Error (NMBE). For the moment, CV(RMSE) has reached a value of about 54.1%, and NMBE has reached 7.2%. These are values well over acceptable limits as presented by ASHRAE, which require that CV(RMSE) should not be more than 15% and that NMBE shall not exceed 5% for a calibrated model. Therefore, to satisfy this, further tuning of key parameters-occupancy schedules, internal heat gains, and weather conditions-will be done. A series of simulations will be performed in order to reduce the discrepancies, bringing the model within acceptable error ranges in conformance with the ASHRAE standards for energy model calibration.

4.CONCLUSION

The present study has developed an energy model for a Mediterranean climate healthcare facility and compared it with one year of actual electricity consumption data. However, the initial calibration results indicate that the values of CV(RMSE) and MBE are outside the acceptable limits, highlighting the need for further refinements. Future work will focus on improving the calibration process to enhance model accuracy, taking into account the specific operational characteristics of the facility to achieve more reliable energy performance predictions.

REFERENCES

[1]   F. Ran, D. ce Gao, X. Zhang, and S. Chen, "A virtual sensor based self-adjusting control for HVAC fast demand response in commercial buildings towards smart grid applications," *Appl Energy*, vol. 269, p. 115103, Jul. 2020, doi: 10.1016/J.APENERGY.2020.115103.

[2]   L. G. Swan and V. I. Ugursal, "Modeling of end-use energy consumption in the residential sector: A review of modeling techniques," *Renewable and Sustainable Energy Reviews*, vol. 13, no. 8, pp. 1819–1835, Oct. 2009, doi: 10.1016/J.RSER.2008.09.033.

[3]   M. Ferrando, F. Causone, T. Hong, and Y. Chen, "Urban building energy modeling (UBEM) tools: A state-of-the-art review of bottom-up physics-based approaches," *Sustain Cities Soc*, vol. 62, p. 102408, Nov. 2020, doi: 10.1016/J.SCS.2020.102408.

[4]   C. F. Reinhart and C. Cerezo Davila, "Urban building energy modeling – A review of a nascent field," *Build Environ*, vol. 97, pp. 196–202, Feb. 2016, doi: 10.1016/J.BUILDENV.2015.12.001.

[5]   A. Sola, C. Corchero, J. Salom, and M. Sanmarti, "Simulation tools to build urban-scale energy models: A review," *Energies (Basel)*, vol. 11, no. 12, 2018, doi: 10.3390/en11123269.

[6]   W. Li *et al.*, "Modeling urban building energy use: A review of modeling approaches and procedures," *Energy*, vol. 141, pp. 2445–2457, Dec. 2017, doi: 10.1016/J.ENERGY.2017.11.071.

[7]   S. Ferrari, F. Zagarella, P. Caputo, and M. Bonomolo, "Assessment of tools for urban energy planning," *Energy*, vol. 176, pp. 544–551, Jun. 2019, doi: 10.1016/J.ENERGY.2019.04.054.

[8]   "hourly weather data."

[9]   F. et al. Parand, *Environmental design. (incorporating corrections as of May 2019)*. Chartered Institution of Building Services Engineers, 2019.

[10]   "Thermal insulation requirements for buildings."

[11]   "testo 635 Humidity/temperature/pressure dew point measuring instrument Instruction manual en."

[12]   ANSI/ASHRAE, "ASHRAE (2014). Guideline 14-2014: Measurement of Energy, Demand, and Water Savings. American Society of Heating, Refrigerating, and Air Conditioning Engineers, Atlanta, Georgia.," vol. 4, 2014, [Online]. Available: https://webstore.ansi.org/standards/ashrae/ashraeguideline142014

DESIGN AND ANALYSIS OF STRETCHABLE LOCKING JOINTS

Elif Zubeyde MERIC[1]
Pınar Aydan DEMIRHAN[2]

[1]*Mechanical Engineer at Samsung Electronics Tekirdağ TÜRKİYE*
[2]*Asst. Prof. at Trakya University Edirne TÜRKİYE*

E-mail: e.meric@samsung.com, pinard@trakya.edu.tr

In this study, flex-lock connections, which is one of the methods of assembling plastic products that we use in almost every aspect of our daily life, with each other or with non-plastic products, were examined. Connection methods of these connections, which take advantage of the flexibility of the parts during assembly and provide significant benefits such as cost advantage and ease of assembly, have been examined. These connection types, their features, application areas and studies on this subject are explained respectively. These connections and their usage areas are explained in detail.

Keywords: Plastic part assembly, Ease of Assembly, Flexible locking connections

1. INTRODUCTION

The use of plastic parts is increasing rapidly every day and is replacing other materials. The fact that production and mold investment are easier and cheaper than sheet metal parts has made plastics preferred. The most suitable connection method for fast and practical use that does not require intensive labor for easy assembly of plastic parts in the industry is flexible snap-on nails. These structures, which are integral with the material without using separate assembly equipment, spending extra time and using the elastic deformation of the material, were first used during the Second World War. In design error type effect analysis studies, which are frequently applied for designs in the industry, the goals of simplifying parts, reducing the number of connectors, facilitating assembly and reducing tool use are emphasized. For mass production, flexible snap-on nail structures are frequently preferred to minimize both time, number of parts, assembly labor and tool use. With the demand for plastics, their connection with other materials has also gained importance. Examples of main plastic part connections are friction welding, vibration welding, bonding, insert connection and flexible locking connections. Within the scope of the study, the types and details of flexible locking connections, their places of use, engineering calculations, usage limits, and approaches that can be used in material selection were examined.

2. MATERIAL AND METHODS

The design was made by following the design rules of flexible lockable connections. NX Unigraphics program was used while making this design. ABS material was used in this study.
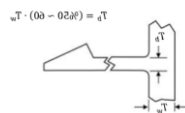
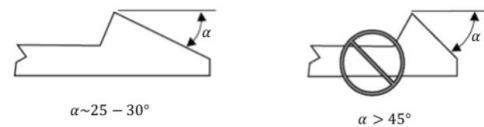**Figure 1.** The ratio of the wall thickness of the beam and its wall
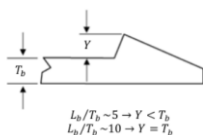
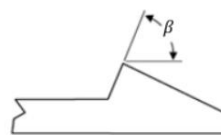**Figure 2.** Mounting surface angle

Figure 3. Depth of attachment surface surface

Figure 4. Angle of the attachment
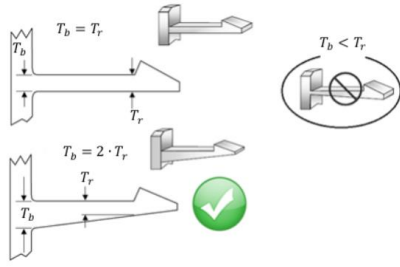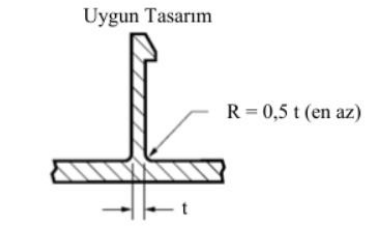
Figure 5. Beam end wall thickness
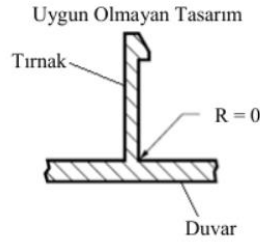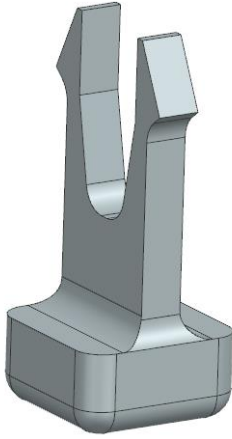

Figure 6. Radius

3. RESULTS

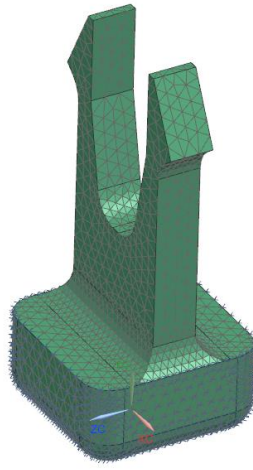**Figure 7.** Flexible locking connection design regions
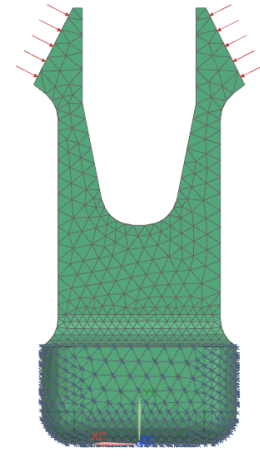

Figure 8. Mesh structure
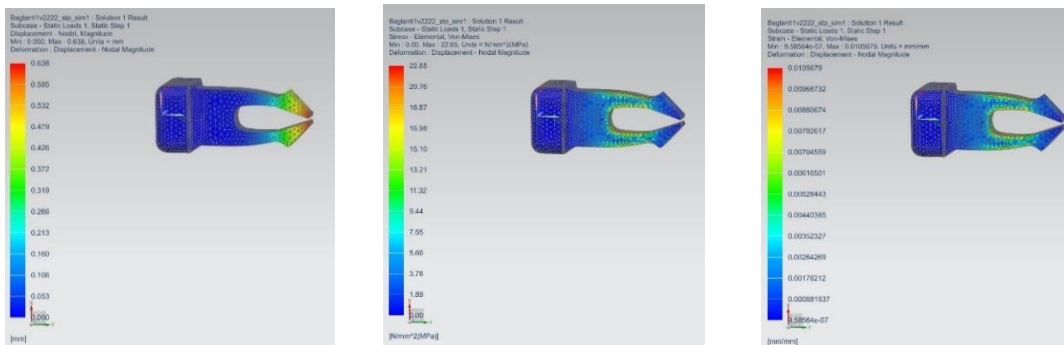

Figure 9. Applied force

Figure 10. The amount of displacement, stress and elongation under 10N force
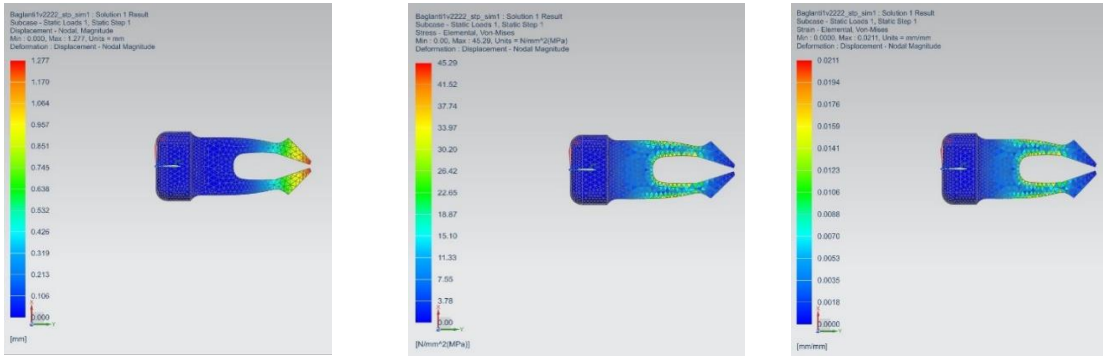
Figure 11. The amount of displacement, stress and elongation under 20N force
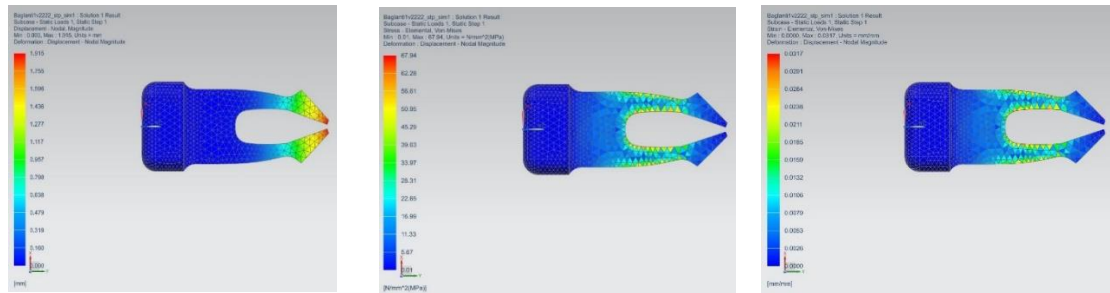
Figure 12. The amount of displacement, stress and elongation under 30N force

4. CONCLUSION

As a result of the the analysis, considering the stress values, the force to be applied for this design was determined as 20N. The part will be deformed at forces applied above 20N.

REFERENCES

[1] Türköz, S. (2006) "Plastik Parçalarda Esneyerek Kilitlenen Bağlantıların Tasarımı". Yüksek Lisans Tezi, Sayfa 1. İstanbul Teknik Üniversitesi Fen Bilimleri Enstitüsü, İstanbul.

[2] Burhan, Ş. (2022) "Seramik Takviyeli Termoplastik Matrisli Kompozitten Üretilen Farklı Snap-Fit Tırnak Tasarımlarının, Nümerik Analizi ve Deneysel (Mekanik ve Mikroyapı) Olarak İncelenmesi". Doktora Tezi, Manisa Celal Bayar Üniversitesi İmalat ve Konstrüksiyon Anabilim Dalı Makine Mühendisliği Bilim Dalı, Manisa.

[3] İnternet: Google Images. Snapfits examples. URL: http://www.webcitation.org/query?url=https%3A%2F%2Fwww.google.com.tr%2Fse

arch%3Fbiw%3D1366%26bih%3D657%26tbm%3Disch%26sa%3D1%26ei%3DnJr mW7rNHuP5qwHQxrKABQ%26q%3Dsnapfits%2Bexamples%26oq%3Dsnapfits%2Bexamples%26gs_l%3Dimg.3...15236.17343.0.17435.9.9.0.0.0.0.178.910.0j6.6.0....0...1c.1.64.img..3.0.0....0.ZwQi96VFJNg.+&date=2019-05-02, Son Erişim Tarihi: 10.11.2018.

[4]   Bonenberger, P.R. (2016). The first snapfits handbook: Creating and managing attachments for plastics parts (Üçüncü Baskı). Munich: Carl Hanser Verlag, 1-268.

[5]   Fulya, E. "(2019) Esneyerek Kilitlenen Bağlantı Elemanlarının Tasarımı Ve Yapay Sinir Ağları (Ysa) İle Modellenmesi" Yüksek Lisans Tezi, Gazi Üniversitesi Fen Bilimleri Enstitüsü, Ankara.

[6]   Nilgün, A. (2013) "Destek Federli Standart Kiriş Tipi Tırnak Yapılarında Sonlu Elemanlar Analizi İle Optimum Tasarımın Bulunması" Yüksek Lisans Tezi, Gazi Üniversitesi Fen Bilimleri Enstitüsü, Ankara.

[7]   "Manufacturing Processes for Plastics." Engineering Resource.

EFFECT OF SURFACTANT CONCENTRATION AND HEAT TREATMENT TEMPERATURE ON HARDNESS AND THİCKNESS OF ELECTROLESS Ni-B-P-B₄C COMPOSITE COATINGS

A.Betül Demir[1], Z. Alı-Zada[2], E. Furkan Erkan[3], İ. Dinç[1], Z. Özcan[1], F. Algül[1], H. Algül[1], M. Uysal[1], S. Tan[1], A. Alp[1]

[1] *Department of Metallurgical and Materials Engineering, Faculty of Engineering, Sakarya University,*
[2] *Department of Environmental Engineering, Faculty of Engineering, Sakarya University,*
[3] *Department of Industry Engineering, Faculty of Engineering, Sakarya University*

E-mail: aysedemir@sakarya.edu.tr

Electroless nickel coatings are intensively studied in the development of aluminum surfaces due to their superior properties. These properties have made the production and research of multiple alloys and composites popular.

In this study, NiBP-B₄C alloy composite coatings were obtained by using two different reducers together on aluminum substrate by chemical reduction method and by depositing B₄C particles together with nickel-boron phosphorus. In order to obtain optimum results in the study, firstly B₄C ceramic particle concentration (10 g/L) was kept constant and the amount of sodium dedosyl sulfate (SDS) surfactant (0.05, 0.1, 0.15) and heat treatment temperature (375°C, 400°C and 425°C) were examined.

Surface and morphological properties of the produced composite coatings were performed by SEM-EDS, XRD. In terms of Hardness and Coating Thickness, optimum values were obtained in the coating bath where the heat treatment temperature was 400°C and the SDS amount was 0.1 g/L, and they were 1006 (Hv) and 26.3 μm, respectively. In the studies, optimum parameters based on surfactant and heat treatment inputs were determined using Taguchi design and L9 orthogonal array. ANOVA analysis was performed by taking into account the interactions of the factors with each other.

Keywords: Electroless Coating, Hardness, Corrosion, Thickness, Taguchi Design.

1. INTRODUCTION

Electroless nickel coating method obtained by chemical reduction of metal ions on a suitable substrate without applying an external electric current.The production of electroless nickel coating is based on the principle that nickel ions are reduced by a reducing effect on the metal surface, which has a catalytic effect, and converted into nickel metal. Since nickel metal itself has a catalytic effect, the reaction continues on the nickel surface after the nickel has turned into a metallic state. The nickel ion required for coating is provided by metal salts in the solution.These ions are reduced to nickel metal by the help of reducers in the solution on the material with catalytic surface.In the meantime, nickel combines with the phosphorus or boron released and forms an alloy [1].

Electroless nickel coating is used to deposit nickel without using electric current. The coating is deposited by an autocatalytic chemical reduction of nickel ions with hypophosphite, amino borane or borohydride compounds.Electroless nickel is an engineering coating used because of its excellent corrosion and wear resistance. Electroless nickel coatings are also applied to aluminum to provide a solderable surface and can be used for lubricating properties in molds.The most commonly applied coating type in electroless coating applications is electroless Ni-P coatings. Electroless Ni-P coating technique is used in many areas because it has excellent coating properties such as high corrosion resistance, wear resistance, good lubricity, high hardness and acceptable ductility. The deposition of composite materials (metallic and non-metallic components) together by electroless method is called electroless composite coatings. Wear-resistant composite coatings can be produced by deposition of fine/small and hard/lubricating particles. Hard particles such as diamond, silicon carbide, aluminum oxide, titanium nitride and polytetrafluoroethylene (PTFE) particles can be produced together with solid lubricants in electroless composite coatings. Other small interparticle metallic compounds and fluorocarbons can be dispersed in the electroless Ni-P/B matrix [2].

Another coating type is electroless Ni-B coatings. Ni-B coatings are produced as an alternative to Cr coatings. Electroless nickel boron coatings are interesting and open to development with their features such as improved hardness and wear behavior [3].

Electroless Coatings: Electroless pure Ni coatings,produced in hydrazine baths:-(97-99% Ni); Electroless–alloy coatings: Ni-P-X composite,Ni-B-X composite,X: Al_2O_3 ZrO_2 SiC PTFE B4C TiN,TiN Graphene etc.Electroless–composite coatings: Alkaline Ni-P,Acidic Ni-P,Low phosphorus 3-5%,Medium phosphorus 6-9%,High phosphorus 10-14%,Alkaline Ni-B,Acidic Ni-B,High boron coating (3-8%),Low boron coatings (0.4-0.5%),Tertiary alloy (Ni-P-B, Ni-W-P etc.) Types of Electroless Coatings: According to the type of reducer in the bath;(hypophosphite,boron

hydride,aminoboron,hydrazine baths.According to the pH of the solution;(alkaline baths,hypophosphite,boron hydride baths,acidic baths,hypophosphite,aminoboron baths [4].

In this study, NiBP-B$_4$C alloy composite coatings were obtained by using two different reducers together on aluminum substrate by chemical reduction method and by depositing B4C particles together with nickel-boron phosphorus. In order to obtain optimum results in the study, firstly B4C ceramic particle concentration (10 g/L) was kept constant, and the amount of sodium dodecyl sulfate (SDS) surfactant (0.05, 0.1, 0.15 g/L) and heat treatment temperature (375°C, 400°C and 425°C) were examined. In this study, Taguchi's Experimental Design will be employed to ascertain the coating bath parameters. Taguchi's Experimental Design method has gained prominence as an effective tool for tackling optimization challenges. This method not only guarantees achieving solutions with a minimal number of experiments but also facilitates the development of superior processes and products across various dimensions. This encompasses minimizing product cost losses by providing necessary tolerances at the lowest cost, reducing test numbers, and evaluating them within the context of an evolving understanding of quality cost (Phadke, 1989).

2. MATERIAL AND METHODS

For the experimental study, 6000 series aluminum alloy with dimensions of 30x30x5 mm was used as a substrate. Bath components; Nickel sulfate was used as nickel source, sodium acetate and lactic acid were used as complexing agents, and thiourea was used as stabilizer.

After the necessary pre-treatments are applied, the base material is immersed in the Ni-P-B-B4C composite coating bath. Coating was carried out for 1 hour at 75 degrees.

1.Table: Bath Components

Bath Components	Concentration
Nickel Source - (NiSO4.6H2O)	33 g/L
Reductant - Sodium Hypophosphite - (C2H3NaO2)	20 g/L
Boranediamine - (C4H12BBrN2)	2 g/L
Sodium Acetate -(C2H3NaO2)	16 g/L
Lactic Acid - (C3H6O3)	28 mL/L
Thiourea - (CH4N2S)	0.001g/L
B4C Powder Concentration	10 g/L
Parameters	
pH	5-6
Time (min)	60
Temperature (ºC)	75-80

The Taguchi method is a statistical technique that enables the design of experiments for optimizing performance characteristics (Taguchi, 1986). Genichi Taguchi introduced an eponymous approach aimed at enhancing the efficiency of conducting and assessing experiments [5].Consequently, preliminary studies conducted prior to the experiment indicated a substantial reduction in the number of required experiments. The primary objective of the Taguchi method revolves around minimizing variability concerning the target value. This approach is rooted in experimental design and incorporates robust design concepts and orthogonal sequences into the fractional factorial experiment design method. The experimental results obtained in the Taguchi Experimental Design method are evaluated by converting them to the Signal/Noise (S/N) ratio. The signal/noise ratio value is calculated and analyzed in different ways according to whether the result value is "the small value is good", "the big value is good", and the nominal value is good". Another important point is that the experimental design is balanced, that is, it allows the factors to be evaluated independently of each other, and in this way, an equal number of samples are made under each tested condition for the different levels of factors in the design. Taguchi's standard designs are built on this system [5].

3. RESULTS AND DISCUSSION

Hardness values are given depending on 3 different heat treatment temperatures. Hardness conditions; 10 g load was applied for 15 seconds. Based on this, the most suitable heat treatment temperature was determined as 400 degrees, 0.1 g/L surfactant. The optimum value was determined as 400 degrees at 3 different heat treatment temperatures. At Figure 1. 400 degrees, at a concentration of 0.1 g/L SDS; the effect of the coating bath on the hardness was observed and the hardness value was determined as 1006 (Hv).
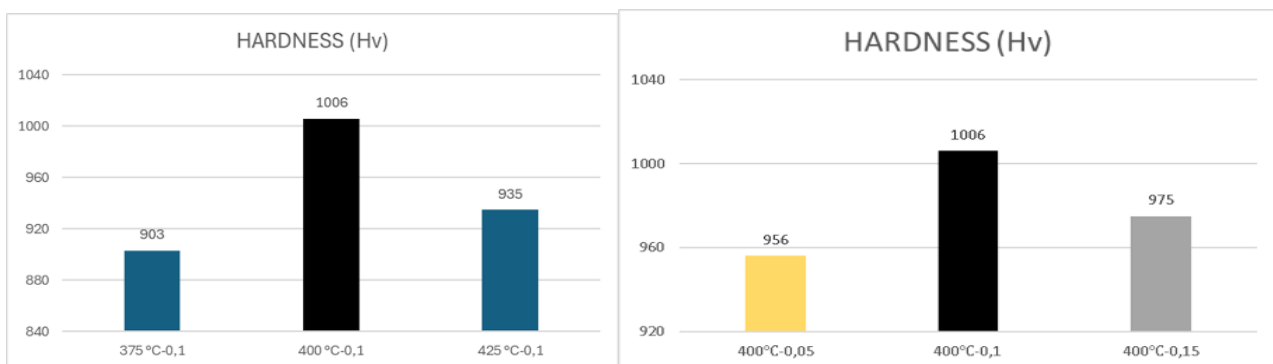

Figure 1. Graph hardeness

It has been determined that the agglomeration of particles in the coating decreases and homogeneity increases depending on the amount of surfactant. From here, it is obvious that the agglomeration of particles can be prevented by adding an amount of surfactant sufficient for the surface area of the particles, depending on the amount of particles added. Kılıç F.,studied the effect of surfactant concentration in Ni-SiC composite coating baths, keeping other parameters constant [5].
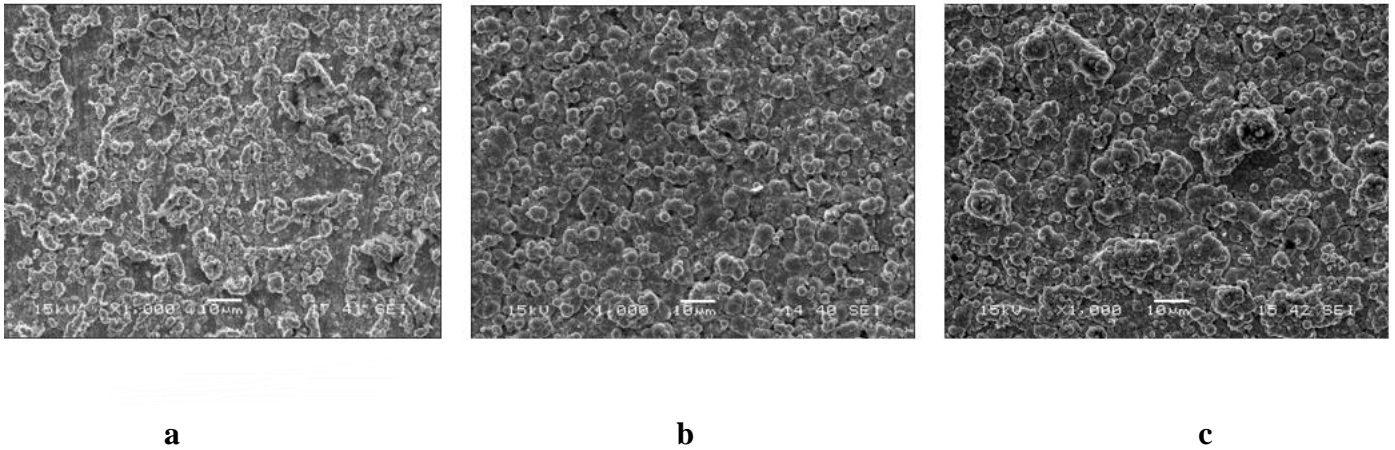

a   b   c

Figure 1.SEM images 400 degree (a.0,05 g/L;b.0,1 g/L;c.0,15 g/L)
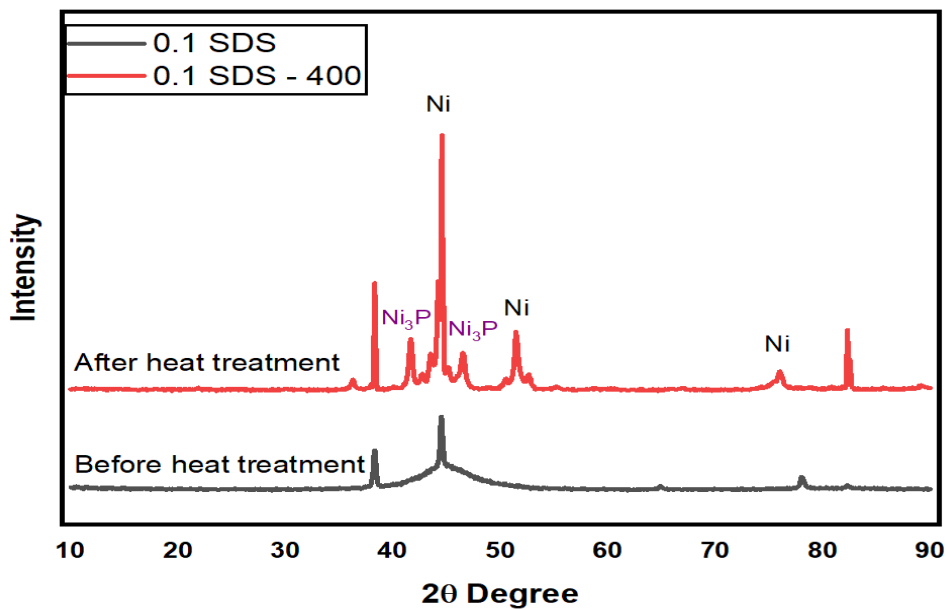
Figure 2. XRD analysis results of Ni-P-B-B4C composite coatings

The XRD analysis results of Ni-P-B-B$_4$C composite coatings before and after heat treatment are given Figure 2.In Ni-P-B-B$_4$C coatings, it is seen that the structure is amorphous before heat treatment. It is seen that the amorphous structure turns into a crystalline structure after heat treatment. After 400 degree heat treatment, there is a phase transformation and Ni$_3$P phases are formed in the structure.

When looking at the graph; the change in the amount of surfactant is seen at 400 degrees heat treatment temperature. The best value was observed at 0.1 g/L SDS.

Figure 3.the coating thickness was determined as **26.3 microns** according to the selected optimum value.
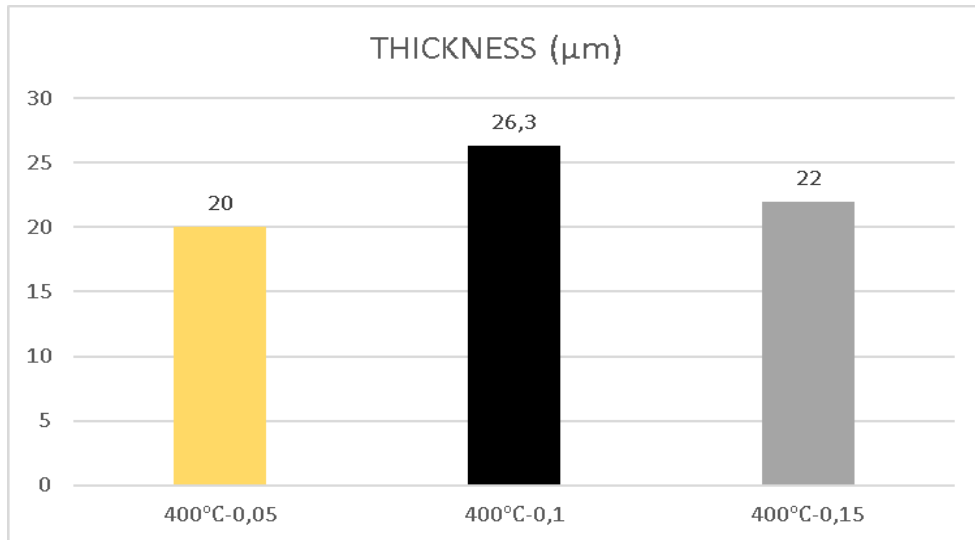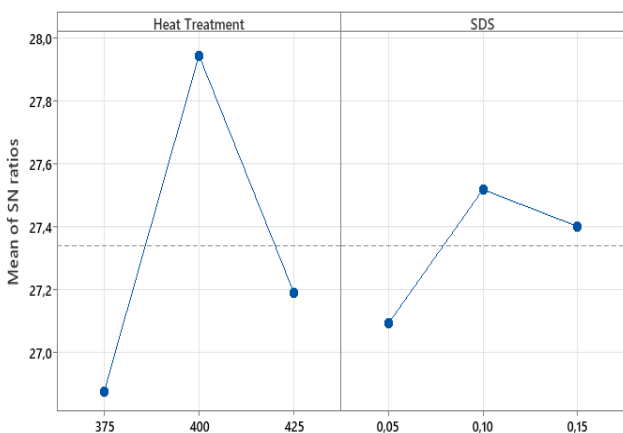

THICKNESS (µm)

Figure 3. Graph thickness

A statistical analysis of variance (ANOVA) was conducted separately for each output parameter to assess the significance of each factor on coating thickness, hardness to determine whether the factors had a significant effect on these outputs. The ANOVA results for thickness, as shown in indicate that heat treatment, while SDS factors variability significantly influence thickness.

Figure 4. shows the Signal to Noise Ratios (SNR) across different levels of Heat Treatment and SDS. The results indicate that Level 2 for both factors achieves the highest SNR, with Heat Treatment at 27.95 and SDS at 27.52, suggesting optimal performance at these levels. The Delta values, 1.07 for Heat Treatment and 0.42 for SDS, show a notable improvement in SNR for Heat Treatment and a more consistent effect for SDS. Consequently, Level 2 for Heat Treatment is ranked highest in enhancing signal quality, with SDS also showing effectiveness, though with less variation. These findings highlight Level 2 as the preferred condition for maximizing SNR. Figure 5. illustrates the Signal to Noise Ratios (SNR) across different levels of Heat Treatment and SDS, with higher values signifying better performance. For Heat Treatment, Level 2 achieves the highest SNR of 27.95, outperforming Levels 1 (26.88) and 3 (27.19), thus proving to be the most effective for enhancing signal quality. Similarly, SDS Level 2 yields the highest SNR at 27.52, although the differences between levels are smaller, as shown by the Delta value of 0.42. The ranking positions Heat Treatment Level 2 as the top performer (Rank 1) and SDS Level 2 in second place (Rank 2). Overall, these

results indicate that Heat Treatment Level 2 is the most effective for maximizing SNR, while SDS also improves performance, albeit to a lesser degree.

Figure 4. Main Effects Plot for SN ratios of Thickness Hardness
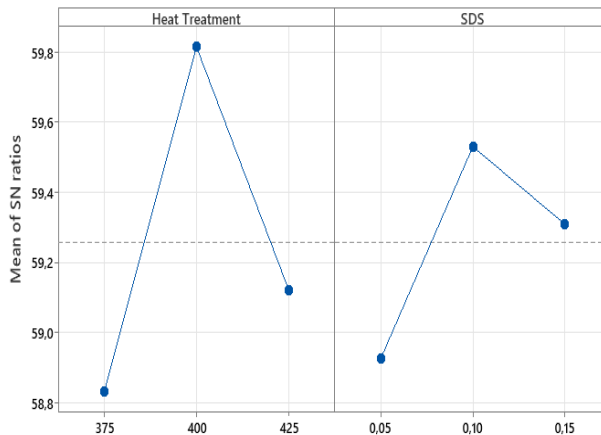
Figure 5. Main Effects Plot for SN ratios of

In addition, the ANOVA results show an R-squared value of 98.65% and an adjusted R-squared value of 97.29% for hardness. The high R-squared value indicates that 98.65% of the variability in the response variable is explained by the model, suggesting an excellent fit. The adjusted R-squared value of 97.29% accounts for the number of predictors in the model and confirms that the model remains robust even after adjusting for the number of variables. These results collectively suggest that the model provides a very accurate prediction of the response variable, with only a small proportion of variability remaining unexplained.

4. CONCLUSION

Optimization of electroless Ni-P-B-B$_4$C alloy composite coating bath was carried out using three different surfactant amounts - SDS (0.05, 0.1, 0.15 g/L). The most suitable SDS amount was determined as 0.1 g/L.

375, 400 and 425; three different heat treatment temperatures were studied and the optimum temperature was determined as 400 degrees.On selected Ni-P-B-B$_4$C composite coatings, the thickness was determined as 26.3 μm.The effect of the coating bath on the hardness was observed and the hardness value was determined as 1006 (Hv).In addition, Taguchi's Experimental Design was used in this study to determine the coating bath parameters.The results show that both heat treatment and surfactant concentration significantly affect the coating hardness, with optimum conditions determined as 400°C for heat treatment and 0.1 g/L for surfactant concentration.

This study,utilized a Taguchi L9 (3^2) orthogonal array to optimize the process parameters for electroless coatings, focusing on the effects of heat treatment and surfactant concentration on coating thickness and hardness. The experimental design revealed that heat treatment and surfactant levels significantly impact hardness but have less influence on thickness. Analysis of variance (ANOVA) indicated that while heat treatment and surfactant concentration had a substantial effect on hardness, it was revealed that 73.08% of the variability in hardness was due to the heat treatment temperature and 25.56% was due to the surfactant concentration. The Signal to Noise Ratios (SNR) analysis further demonstrated that Level 2 for heat treatment and surfactant concentration offered the optimal performance.The high R-squared values (98.65% for R-squared and 97.29% for adjusted R-squared) ,indicating a robust model fit for hardness. Overall, the findings underscore the importance of precise heat treatment and surfactant adjustments to enhance coating hardness, while suggesting further exploration is required to fully understand the factors affecting coating thickness.

ACKNOWLEDGMENTS

REFERENCES

[1] Balaraju, J.N., Sankara Narayanan, T.S.N., Seshadri, S.K., Electroless Ni-P composite coatings. J. Appl. Electrochem., 33, 807–816, 2003.

[2] Agarwala, R.C., Agarwala, V., Electroless alloy / composite coatings : A review. Sadhana, 28, 475–493, 2003.

[3] Brenner, A., Riddell, G.E., Nickel plating on steel by chemical reduction. J. Res. Natl. Bur. Stand., 37, 31–34, 1946.

[4] Brenner, A., Electrodeposition of Alloys: Principles and practice, 2. Academic Press, 1–656, 1963.

[5] Ross, P.J., 1995. Taguchi Techniques for Quality Engineering, 2nd edition. ed. McGraw-Hill Professional, New York

[6]Kılıç, F. (2009). Elektrolitik nano SiC Partikül Takviyeli Nikel Kompozitlerinin Özellikleri (Order No. 29173015).

THE EFFECT OF BORIDING TEMPERATURE ON THE MORPHOLOGICAL AND STRUCTURAL PROPERTIES OF RAMOR 500 STEEL

Selçuk ATASOY[1], Hasan Onur TAN[1] and Sıtkı AKTAŞ[1]

[1]Department of Mechanical Engineering, Giresun University, Giresun, TÜRKİYE

E-mail: selcuk.atasoy@giresun.edu.tr

Ramor 500 armor steel is categorized as a high-strength ballistic protection steel, featuring a hardness range of 490 to 560 HV and thicknesses typically from 2 to 30 mm. It is specifically designed to endure high-velocity impacts. Boriding is a thermo-chemical process that involves the diffusion of boron, creating a hard surface coating composed of mixed boron compounds, depending on the substrate material. In this study, a thermo-chemical coating method known as box boriding was used to boride Ramor 500 steel, performing at 900 °C, 950 °C, and 1000 °C for 4 hours. The structural and morphological properties of borided Ramor 500 were examined using scanning electron microscopy (SEM), energy-dispersive X-ray spectroscopy (EDS) and profilometer. The boride layer thickness, microhardness values and structural characteristics of the steels were compared based on the boriding temperature. As a result, higher boriding temperatures led to increased surface roughness and microhardness values for the steel and thicker boride layers.

Keywords: Boriding, Boriding temperature, Ramor 500 steel, mechanical properties

1. INTRODUCTION

Ramor 500 armor steels are widely used, particularly in the defence industry, due to their high hardness and superior strength properties, which provide anti-ballistic capabilities [1,2]. However, in some applications, these steels have limitations in terms of toughness, which is critical for durability and impact resistance. The high hardness of the steel can lead to a decrease in toughness [3]. This relationship between hardness and toughness plays a significant role in the material's ability to withstand sudden impacts or dynamic loads, especially under service conditions [4].

In most engineering applications, materials are expected to have surfaces resistant to wear while also being resilient against impact loads arising from service conditions. Additionally, while hard coatings applied to material surfaces provide increased wear resistance, they tend to be prone to cracking under concentrated loads [5].

The balance between hardness and toughness in Ramor 500 steel is a critical factor for its application in environments that require both wear resistance and impact durability. While high hardness benefits wear resistance, it is essential to optimize the microstructure and alloying elements to maintain sufficient toughness. This balance ensures that materials like Ramor 500 steel can effectively withstand sudden impacts and dynamic loading conditions, making them suitable for demanding applications [6].

Surface hardening treatments are crucial for enhancing the wear and impact resistance of materials like Ramor 500, a high-strength steel used in ballistic protection. Some of the methods applied for surface hardening include nitriding and carbonitriding [7], ion bombardment and coating [8], and laser surface hardening [9]. Laser surface hardening is a precise method that uses laser beams to heat the metal surface, followed by rapid cooling, which increases hardness without affecting core properties [9]. Ion bombardment, followed by the deposition of a reactive metal coating and additional ion bombardment, can create hard materials such as carbides or nitrides on the surface. This technique enhances surface hardness through radiation-enhanced diffusion [8]. The nitriding and carbonitriding process involves treating the metal at high temperatures in a nitrogen-rich atmosphere to form a hard nitride layer on the surface. The addition of nitrous oxide accelerates the process, making it efficient for steel components [7].

Another surface hardening process applied to steel materials is boriding, a thermo-chemical surface treatment technique conducted at high temperatures. Boriding is one of the most effective methods for improving the surface performance of steels. Compared to other coating methods, such as carburizing and nitriding, boriding provides significantly higher hardness and wear resistance.

Through this process, the surface hardness of the material can increase up to tenfold, depending on the material type, for example, in iron. The process is typically conducted at temperatures ranging from 700 to 1100°C for 1 to 12 hours and can be applied in various mediums, such as solid, liquid, gas, paste, plasma, or plasma paste. Boriding can be applied not only to steels but also to non-ferrous metals and alloys. As a result of this high-temperature process, single-phase (FeB/Fe_2B) or dual-phase (Fe_2B+FeB) metal borides form on the iron surface. The layer formed by these phases can either exhibit a sawtooth-like structure when combined with the diffusion zone or present a more uniform structure. Among the boriding methods, pack boriding stands out due to its lower cost and ease of application compared to other processes. This method involves embedding the metal in a boron-containing powder, heating it to high temperatures, and allowing boron atoms to diffuse into the metal surface.

In this study, depending on boriding temperature on the structural and mechanical properties of Ramor 500 armor steel were investigated by applying pack boriding treatment at 900, 950, and 1000°C for 4 hours.

2. MATERIAL AND METHODS

In this study, Ramor 500 armor steel with dimensions of 20 x 20 mm was used and its chemical composition is provided in Table 1. The surfaces of the test specimens were polished using SiC abrasive papers with grit sizes of 80, 150, 360, 500, 800, and 1200, respectively. The boriding process was carried out using the pack boriding method with commercial Ekabor II powder. The samples were placed into Ekabor II powder inside a cylindrical stainless steel crucible. Before placing the crucibles, the furnace was heated to 900°C, 950°C, and 1000°C, and the samples were borided in a preheated furnace for 4 hours. They were then left to cool at room temperature. After the boriding process, the cross-sections of borided samples were polished with SiC abrasive papers followed by 3 µm and 1 µm diamond suspensions, and then cleaned in alcohol before being etched in a 5% Nital solution to determine the boride layer thickness. The etched samples were examined using a scanning electron microscope (SEM) (ZEISS EVO LS 10) to determine the thickness of the boride layer. In addition, the elemental composition of the samples was revealed using energy-dispersive X-ray spectroscopy (EDS). Microhardness measurements were performed using the Vickers method under a 200 g load and at intervals of 20 µm (LAIHUA HVS 1000B). At least five measurements were taken for these tests, and the average value was calculated.

3. RESULTS AND DISCUSSION

The cross-sectional SEM images and The EDS results of the Ramor 500 armor steels subjected to boriding at 900°C, 950°C, and 1000°C for 4 hours are presented in Figure 1 and Figure 2, respectively. The measured boride layer thicknesses obtained from the cross-sectrional SEM images are provided in Table 2. When the boride layer thicknesses are examined based on boriding temperature, it is observed that after boriding at 900°C, 950°C, and 1000°C for 4 hours, the boride layer thicknesses were measured as 95.2 μm, 110.1 μm, and 140.2 μm, respectively. It was observed that the boride layer thicknesses increased with the increase of boriding temperature, with the highest layer thickness obtained at boriding at 1000°C for 4 hours. Moreover, it was noted that the boride layers exhibited a sawtooth morphology. This phenomenon can be explained by the diffusion of boron atoms into the base material. Furthermore, the EDS results also indicate that boron has diffused. As is well known, the diffusion rate increases as temperature and duration rise, resulting in increased boride layer thicknesses [10-14].

Table 1. The chemical composition and mechanical properties of Ramor 500 armor steel.

C	Si	Mn	P	S	Cr	Ni	Mo	B
0.32	0.70	1.5	0.015	0.005	1.0	2.0	0.70	0.005

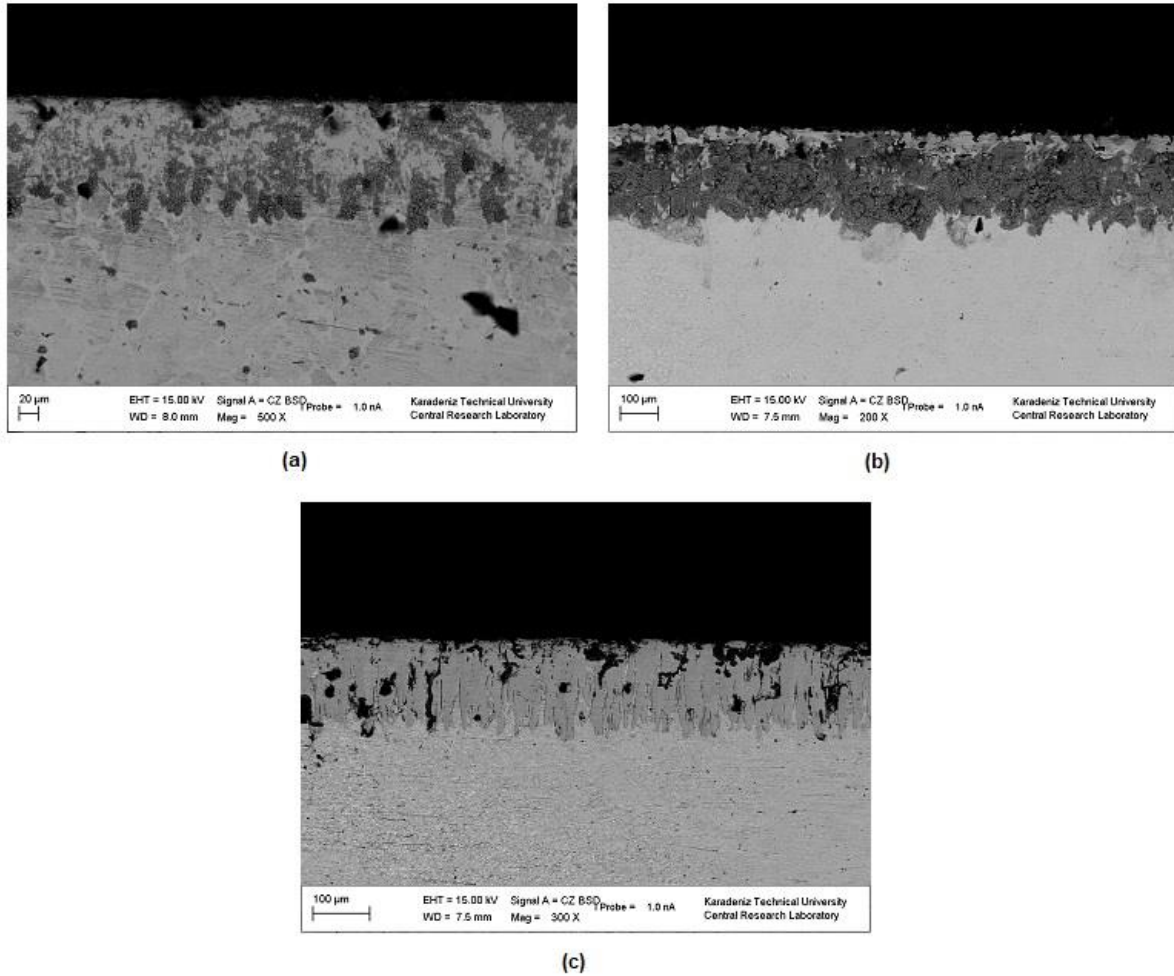| Yield strength (MPa)	Tensile strength (MPa)	Elongation to fracture (%)	Hardness (HBW)	Impact energy (J)
1450	1700	7	480-560	20

Figure 1. SEM images of Ramor 500 armor steel borided at (a) 900°C, (b) 950°C and (c) 1000°C for 4 hours.

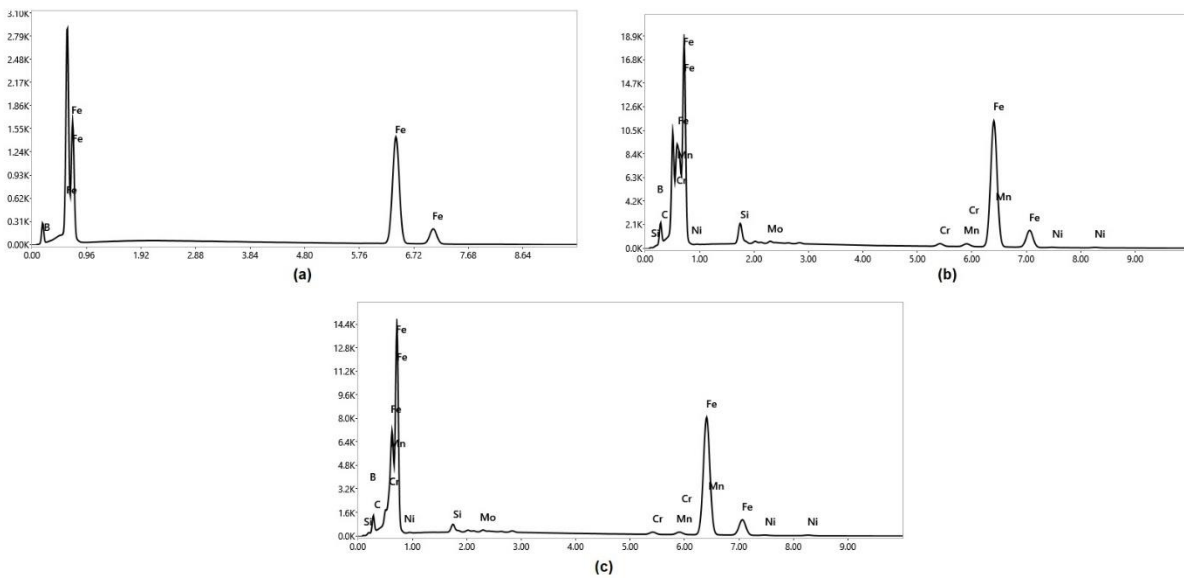**Figure 2.** EDS graphs of of Ramor 500 armor steel borided at (a) 900°C, (b) 950°C and (c) 1000°C for 4 hours.
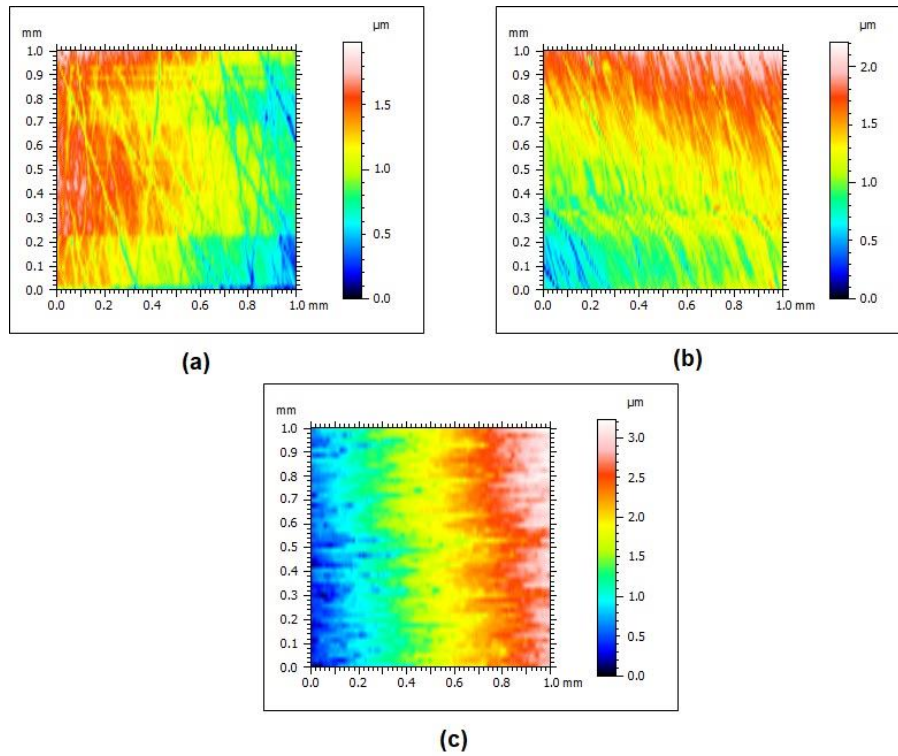
Figure 3. Profilometer results of of Ramor 500 armor steel borided at (a) 900°C, (b) 950°C and (c) 1000°C for 4 hours.

Table 2. The boride layer thickness values of Ramor 500 armor steel borided at different temperatures.

Boriding temperature (°C)	Boriding time (hour)	Thickness of borided layer (µm)
900	4	95.2
950	4	110.1
1000	4	140.2

.

The curves showing the variation in microhardness values of the samples borided at different temperatures with respect to depth are presented in Figure 4. The hardness values of the borided layer range between 260 HV and 2200 HV. As seen in Figure 4, it is observed that the hardness values of the borided samples decrease from the surface towards the interior. Additionally, the hardness of the boride layer formed on the surface increases with the increase in boriding temperature.
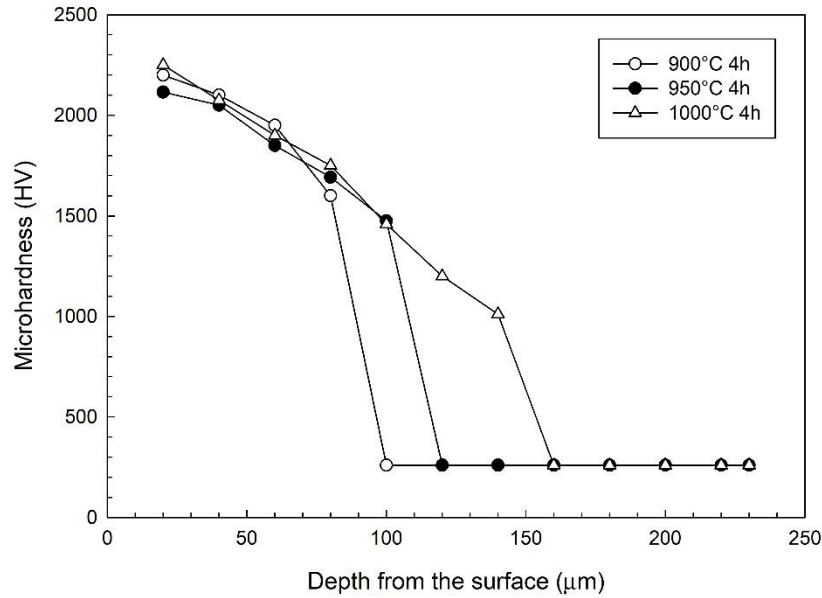
Figure 4. Microhardness versus depth curves for Ramor 500 armor steel borided at different temperatures.

4. CONCLUSION

The phase structure, boride layer thickness, and microhardness values of Ramor 500 armor steel subjected to boriding at different temperatures for 4 hours were examined in relation to the boriding temperature. It was determined that with an increase in boriding temperature, the layer thickness increased from 95.2 µm to 140.2 µm. Additionally, EDX analysis of Ramor 500 armor steel borided for different durations revealed that the boron content increased by increasing the boriding temperature. Based on the SEM, EDX and profilometer results, it was concluded that boron diffused into the Ramor 500 armor steel, and the diffusion depth increased with rising temperature. Furthermore, when the change in microhardness values with respect to temperature was examined, it was concluded that the increased layer thickness due to boron diffusion resulted in an increase in surface hardness.

ACKNOWLEDGMENTS

REFERENCES

[1] Ramor 500 Çeliğinde Isıl İşlemin Mikroyapı, Mikrosertlik ve Abrasiv Aşınma Direncine Etkisinin Taguchi Metoduyla Değerlendirilmesi, (Sep. 30, 2019). doi: 10.17798/BITLISFEN.532073.

[2] S. Taskaya, A. Kaya Gur, and C. Ozay, 'Joining of Ramor 500 Steel with SAW (Submerged Arc Welding) and its Evaluation of Thermomechanical Analysis in ANSYS Package Software', Therm. Sci. Eng. Prog., vol. 13, p. 100396, Oct. 2019, doi: 10.1016/j.tsep.2019.100396.

[3] M. L. Bekci, B. H. Canpolat, E. Usta, M. S. Güler, and Ö. N. Cora, 'Ballistic performances of Ramor 500 and Ramor 550 armor steels at mono and bilayered plate configurations', Eng. Sci. Technol. Int. J., vol. 24, no. 4, pp. 990–995, Aug. 2021, doi: 10.1016/j.jestch.2021.01.001.

[4] İ. Memis and R. Karakuzu, 'High-velocity impact performance of Ramor 500 armor steel', Mater. Test., vol. 64, no. 7, pp. 991–1001, Jul. 2022, doi: 10.1515/mt-2022-0035.

[5] B. R. Lawn et al., 'Damage-Resistant Brittle Coatings', Adv. Eng. Mater., vol. 2, no. 11, pp. 745–748, 2000, doi: 10.1002/1527-2648(200011)2:11<745::AID-ADEM745>3.0.CO;2-E.

[6] Production of high hardness wear resistant steel excellent in low temperature toughness, (Jul. 29, 1994). Accessed: Sep. 24, 2024. [Online Video]. Available: https://typeset.io/papers/production-of-high-hardness-wear-resistant-steel-excellent-3kp83y3yt7

[7] Surface hardening process for metal parts, (Mar. 17, 1983). Accessed: Sep. 24, 2024. [Online Video]. Available: https://patents.google.com/patent/US4531984A/en

[8] Surface treatment of metals, (Sep. 09, 1985). Accessed: Sep. 24, 2024. [Online Video]. Available: https://www.sciencedirect.com/topics/engineering/surface-treatment-of-metal

[9] Lasers in surface engineering, (Jan. 01, 1998). Accessed: Sep. 24, 2024. Available: https://books.google.com.tr/books?id=

[10] Gunes I. Kinetics of borided gear steels. Sadhana-Acad P Eng S. 2013;38(3):527-41.

[11] Gunes I. Wear Behaviour of Plasma Paste Boronized of AISI 8620 Steel with Borax and BO Paste Mixtures. J Mater Sci Technol. 2013;29(7):662-8.

[12] Bican O, Bayca SU, Ocak-Araz S, Yamaneli B, Tanis NA. Effects of the Boriding Process and of Quenching and Tempering after Boriding on the Microstructure, Hardness and Wear of Aisi 5140 Steel. Surf Rev Lett. 2020;27(6).

[13] Keddam M, Chentouf SM. A diffusion model for describing the bilayer growth (FeB/Fe$_2$B) during the iron powder-pack boriding. Appl Surf Sci. 2005;252(2):393-9.

[14] Prince M, Raj GS, Kumar DY, Gopalakrishnan P. Boriding of Steels: Improvement of Mechanical Properties - a Review. High Temp Mater P-Us. 2022;26(2):43-89.

THE EFFECT OF THE DESIGN DIFFERENCES ON HEAT TRANSFER IN ALUMINIUM ALLOY INTERNALLY FINNED TUBES

O. Salcı[1], M.K. Büyükakın[2], S. Öztuna [3]

[1, 2, 3] Mechanical Engineering Department, Faculty of Engineering, Trakya University, Edirne, TÜRKİYE

E-mail: onursalci76@trakya.edu.tr

Energy demand relies on heat energy used in different sectors such as industry, transportation, and domestic heating. The energy efficiency emerges as a critical requirement in buildings for a sustainable energy future. The effective and efficient use of heat energy offers significant environmental and economic benefits.

In this study, the heat transfer performance and useful thermal efficiency of aluminium alloy internally finned tubes with different designs, manufactured by extrusion and used to enhance the useful thermal efficiency of condensing boiler heat exchangers, were investigated.

Al 1070 was used as the heat exchanger tube material. The fluid passing through the inside of the tube is hot flue gas released by the combustion of natural gas with 30% excess air, while the fluid passing around the outside of the tube is water. The hot flue gases cool down due to the impact of the internal fins within the tube, which enhance flow turbulence and heat transfer, and as a result, the water outside the tube is heated. Increasing the rate of cooling in heat exchangers enhances the useful thermal efficiency of condensing boilers, leading to reduced fuel consumption to meet heat demand.

In the numerical calculations, the results obtained using Fluent codes were compared with experimental data. In the experimental studies, the thermal efficiency was calculated by measuring the inlet and outlet temperatures of the flue gas and water in the heat exchanger. Flue gases were released to the heat exchanger internal finned tube by using premixed gas burner in the experimental studies. Geometric optimizations, a design for internally finned heat exchanger tubes with high thermal efficiency (96.2 %) was developed, which can be produced by extrusion and does not experience melting or deformation when exposed to hot flue gases.

1. INTRODUCTION

Aluminium alloy internal finned heat exchanger tubes have emerged as a critical component in modern thermal management systems due to their unique combination of high thermal conductivity, lightweight properties, and enhanced heat transfer capabilities. These tubes are particularly favoured in industries where both efficiency and weight reduction are crucial [1-2]. The high thermal conductivity of aluminium alloys significantly contributes to the efficient transfer of heat, making them superior to other materials like steel in heat exchanger applications [3]. Furthermore, the internal fins integrated into these tubes increase the internal surface area and induce turbulence in the fluid flow, which enhances the convective heat transfer coefficient and overall heat exchanger performance [4-5].

The design of the internal fins can be optimized for various operational conditions, enabling these tubes to be tailored for specific applications [6-7]. The use of aluminium alloys in these tubes also offers excellent resistance to corrosion, further extending their operational life in harsh environments [8-9].

Development of new aluminium alloys with added elements like silicon and magnesium has improved the mechanical properties and corrosion resistance of these tubes, making them even more robust and reliable [10-11]. Additionally, innovations in manufacturing techniques, such as precision extrusion and advanced brazing methods, have allowed for the production of more complex and finely tuned fin structures, which are essential for optimizing heat transfer in compact and high-performance systems [12-13]. Despite these advancements, several challenges remain in the design and application of aluminium alloy internal finned tubes. One significant challenge is the potential for increased pressure drop due to the presence of internal fins, which can lead to higher pumping power requirements and reduced overall system efficiency if not properly managed [5]. Moreover, as the demand for more efficient and compact heat exchangers continues to grow, ongoing research is focused on developing new alloy compositions and fin geometries that can further enhance the performance of these tubes [5-9]. Computational fluid dynamics (CFD) modelling has become an invaluable tool in this research, allowing engineers to simulate and optimize the thermal performance of various designs before physical prototypes are manufactured [14].

2. MATERIAL AND METHODS

Experiments of the study have been conducted in the R&D laboratory of Termo Isı Sistemleri San. ve Tic. A.Ş., located in Tekirdağ, Türkiye, using a water cooling condensing boiler experimental system (Figure 1). The combustion experimental system includes a natural gas line, PWM combustion air fan, premixed burner, heat exchanger, cooling air inlets and outlets. Pre-checks and safety controls were done before each experiment. Natural gas fuel was consumed in the premix burner. Natural gas was supplied by Çordaş Çorlu NG Distribution Co. and the compositional values of natural gas used in the experiments are given in Table 1. Natural gas volumetric flow rate was measured of 1.42 Nm³/h in the premix burner gas fuel inlet. Heat input of 13.6 kW was applied in the combustion experiments with constant λ (excess air ratio) of 1.3. The combustion air temperature and gas temperature were measured as 30 °C and 27 °C, respectively. Flue gas inlet temperature were measured as analog value, which was about 984 °C. Each combustion experiment took 1200 seconds. Flue gas outlet temperature were measured for calculating thermal efficiency. Natural gas flow rate and cooling water flow rate were measured for heat input and output. Cooling water inlet temperature and outlet temperature were measured for calculating heat output.

Table 1. Natural gas compositions [15].

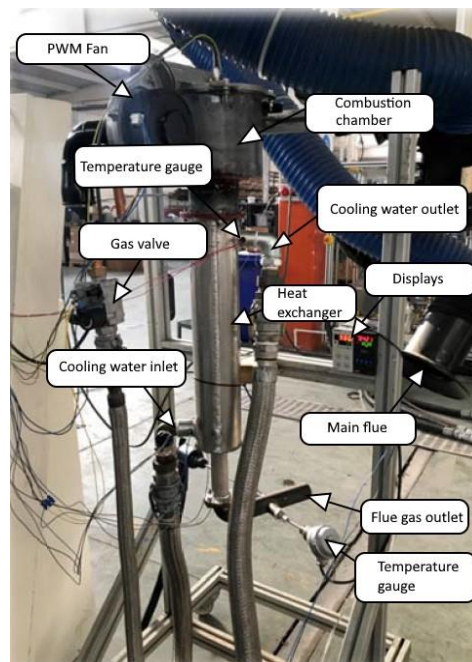| Content	CH_4	C_2H_6	C_3H_8	C_4H_{10}	C_5H_{12}	C_6H_{14}	N_2	CO_2
Mole (%)	96.068	2.198	0.654	0.194	0.0131	0.01	0.668	0.0177

Figure 1. Water cooling condensing boiler experimental system

Al 1070 alloy were used as heat exchanger pipe material. It is known for its high purity, containing 96.975 % aluminium (Table 2.). This composition gives it excellent corrosion resistance, making it ideal for applications exposed to harsh environments. It has also thermal conductivity make it a preferred choice in heat transfer applications. With good workability, Al 1070 is easy to form and process. Cold extrusion method was used for manufacturing in the present study.

The proportion of elements of Al 1070 were given in Table 2. Physical properties of Al 1070 (Table 3.) alloy were calculated according to elements proportions regarding to the physical properties of elements.

Table 2. Al 1070 alloy element proportions

Al	Ti	Si	Mn	Cr	Zn	Mg	Fe	Cu
96.975	0.1	0.3	0.75	0.75	0.125	0.35	0.1	0,55

Table 3. Physical properties of Al1070 alloy [16].

Thermal conductivity (k)	234.033	W/m K
Specific heat (cₚ)	891	J/kg K
Density (ρ)	2813.27	kg/m³
Melting point (Tm)	950.4	K
Thermal diffusivity coefficient (α)	95.7	$(\alpha \times 10^5)$,m²/s
Emissivity (ε)	0.096	

Numerical studies were conducted by using Fluent codes. Continuity, energy, radiative transfer equation, turbulence and conservation of momentum equations were solved for modelling of flue gas and water flow and heat transfer. These equations are given between Eq. (1) and Eq. (6), respectively [17].

Continuity equation:

$$\frac{\delta\rho}{\delta t} + \nabla.(\rho\vec{v}) = 0$$

(1)

Conservation of momentum:

$$\frac{\delta\rho}{\delta t}(\rho\vec{v}) + \nabla.(\vec{v}\vec{v}) = -\nabla p + \nabla(\bar{\bar{\tau}}) + \rho\vec{g} + \vec{F}$$

Energy equation:

$$\frac{\delta}{\delta x_j}\left(\rho u_j h + F_{hj}\right) = u_j \frac{\delta p}{\delta x_j} + \tau_{ij} \frac{\delta u_i}{\delta x_j}$$

(3)

Radiative transfer equation:

$$\nabla.I(\vec{r},\vec{s})\vec{s} + (a + \sigma_s)I(\vec{r},\vec{s}) = an^2 \frac{\sigma T^4}{\pi} + \frac{\sigma_s}{4\pi}\int_0^{4\pi} I(\vec{r},\vec{s}')\Phi\,(\vec{s},\vec{s}')d\Omega'$$

(4)

Turbulence kinetic energy:

$$\frac{\partial}{\partial t}(\rho k) + \frac{\partial}{\partial x_j}\left(\rho k u_j\right) = \frac{\partial}{\partial x_j}\left[\left(\mu + \frac{\mu_t}{\sigma_k}\right)\frac{\partial k}{\partial x_j}\right] + G_k + G_b - \rho\epsilon - Y_M + S_k$$

(5)

Turbulence dissipation rate:

$$\frac{\partial}{\partial t}(\rho\varepsilon) + \frac{\partial}{\partial x_j}\left(\rho\varepsilon u_j\right) = \frac{\partial}{\partial x_j}\left[\left(\mu + \frac{\mu_t}{\sigma_\varepsilon}\right)\frac{\partial k}{\partial x_j}\right] + \rho C_1 S_\varepsilon - \rho C_2 \frac{\varepsilon^2}{k+\sqrt{\upsilon\varepsilon}} + C_{1\varepsilon}\frac{\varepsilon}{k}C_{3\varepsilon}G_b + S_\varepsilon$$

(6)

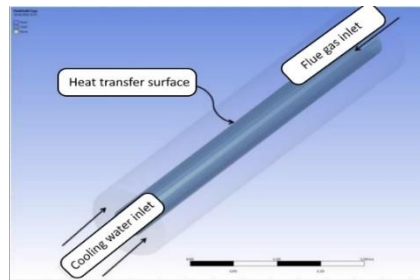Heat transfer surface, cooling water and flue gas inlets of 3D geometry model are shown in Figure. 2.

Figure 2. 3D Geometry model

Two different prototypes of internal finned tube were used in present study. These prototypes are given in Figure 3. Prototype-1 is single piece and Prototype-2 is double piece as left and right one. Internal fins were designed to increase flue gas turbulence and heat transfer performance.
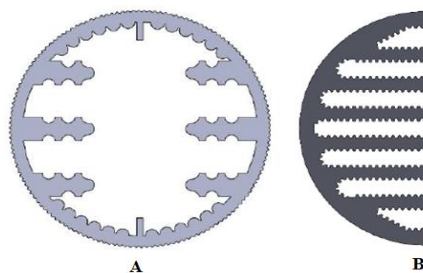

Figure 3. Prototype-1 (A) and Prototype-2 (B)

CFD model mesh properties are polyhedral and hexahedral cell types with 79,868,722 cells and 19,752,319 nodes. The maximum skewness is 0.85. The meshing model is given in Figure 4. The mesh of total geometry was divided into 4 quarters and taken one of quarters for modelling by using symmetry planes.

Mixing species in flue gas were modelled by Species Transport, EDM (Eddy dissipation model). Radiative heat transfer was modelled by DO (Discrete ordinates) model. Flue gas and water turbulence were modelled k-ε turbulence model. Realizable and enhancement wall function were used in turbulence modelling.

Flue gas physical properties are calculated according to different temperatures in the Table 4. These values were used in CFD cases as analysis inputs.
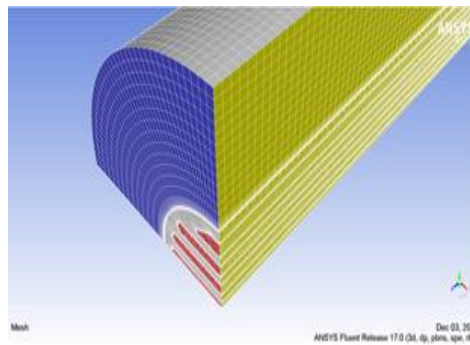

Figure 4. The meshing model

Table 4. Physical properties of Natural gas flue gases at λ:1.3 [18].

Temperature (K)	Density (kg/m³)	Specific Heat (J/kg K)	Thermal Conductivity (W/m K)	Dynamic Viscosity (kg/m.sx10⁵)
273.15	1.246	1136.017	0.022	1.524
323.15	1.053	1145.024	0.026	1.752
373.15	0.912	1150.246	0.029	1.970
423.15	0.804	1158.672	0.033	2.177
473.15	0.719	1171.347	0.036	2.373
573.15	0.593	1201.384	0.043	2.741
673.15	0.505	1234.961	0.049	3.078
773.15	0.440	1268.014	0.056	3.389
1273.15	0.267	1398.545	0.089	4.691
1773.15	0.191	1482.926	0.131	5.867

3. RESULTS AND DISCUSSION

The comparison of numerical calculations and experimental values in the present study is given in Table 5. Experimental and numerical results validated each other with low deviation rates. Experimental and numerical results conducted with natural gas premixed combustion at $\lambda=1.3$ and differences of flue gas inlet and outlet temperatures, cooling water inlet and outlet temperatures have been examined. Flue gas inlet temperature is a reference criteria of 984 °C for all experiments and numerical calculations. Flue gas outlet temperature of Prototype-1 is 11.3 times higher than Prototype-2. Internal fins of Prototype-2 are more enhanced than Prototype-1. Therefore, the thermal efficiency of Prototype-2 is 70% higher than Prototype-1.

Cooling water flow and heating performance is important to calculate heat exchanger performance. Cooling water inlet temperature was taken almost constant with small fluctuations. Although heat inputs were same for all studies, heat outputs were 70% lower than Prototype-2.

Table 5. Comparison of experimental and numerical values

Values	Prototype-1 (Experimental)	Prototype-1 (Numerical)	Prototype-2 (Experimental)	Prototype-2 (Numerical)
Flue gas inlet temperature (°C)	984	984	984	984
Flue gas outlet temperature (°C)	429	441	38	43
Cooling water inlet temperature (°C)	26.88	26.84	26.86	26.81
Cooling water outlet temperature (°C)	28.23	28.12	29.4	29.37
Heat input (W)	7.43	7.38	7.41	7.39
Heat output (W)	4.20	4.07	7.13	7.06
Thermal efficiency (%)	56.5	55.2	96.2	95.6

Temperature contours are given in Figure 5. Cooling performance of Prototype-2 is better than Prototype-1. Flue gas temperature decreases and cooling water is heated up rapidly, accordingly. Heating performance of Prototype-1 becomes low, since hot flue gases flows in the center line of the Prototype-1.
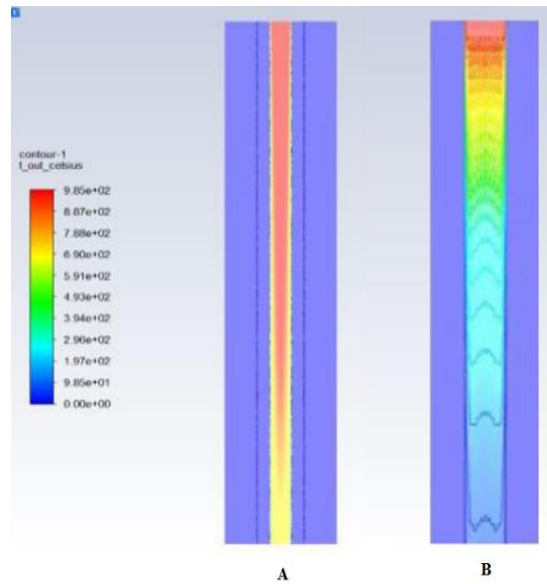
Figure 5. Temperature (°C) contours for Prototype-1 (A) and Prototype-2 (B)

Velocity magnitude contours are given in Figure 6. Although flue gases in Prototype-1 flows faster without having much heat transfer to the cooling water, flue gases in Prototype-2 flows gradually transferring more heat to the cooling water.
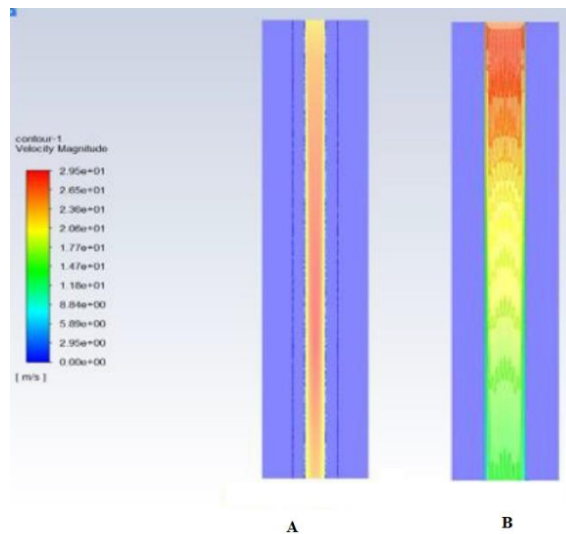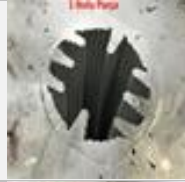

Figure 6. Velocity magnitude (m/s) contours for Prototype-1 (A) and Prototype-2 (B)

Melting of prototypes were controlled in the experimental studies in Table 6. Both prototypes performed good results during the experiments without melting.

Table 6. Comparison of melting performance in experiments

Prototypes	Before experiment	After experiment
Prototype-1		
Prototype-2		

In the present study, Prototype-2 has high thermal efficiency and good heat transfer performance. Prototype-2 can be manufactured in cold extrusion processes. Non-melting performance gives an opportunity for using in heat exchangers as a main material.

4. CONCLUSION

Energy efficiency and fuel saving are very important issue. Increasing heat transfer performance of heat exchangers is eco-friendly application to reduce carbon and pollutant emissions. Additionally, decreasing of fuel consumption at same heat demand provides low fuel costs.

Aluminium alloys have many different applications in industry. Heat exchangers are only one of these applications. In the present study, design changes of 1070 aluminium alloy internal finned heat exchanger tube geometry affect flue gas flow turbulence and heat transfer rate. Increased flue gas turbulence and flow resistance provided rapid heat transfer. High performance heat exchanger pipes gives an advantage to design high efficient compact design.

ACKNOWLEDGMENTS

REFERENCES

[1] Kakac, S., & Liu, H. (2002). Heat exchangers: Selection, rating, and thermal design (2nd ed.). CRC Press.

[2] Wang, C. C., Lee, C. J., & Sheu, W. J. (2015). Performance assessment of aluminum internal finned tubes under various airside and refrigerant conditions. International Journal of Refrigeration, 53, 72-79.

[3] Kuppan, T. (2000). Heat exchanger design handbook. CRC Press.

[4] Liu, Z., Huang, S., & Zhou, Y. (2018). Experimental study on heat transfer characteristics of aluminum alloy internally finned tubes. International Journal of Heat and Mass Transfer, 127, 363-373.

[5] Manglik, R. M., & Bergles, A. E. (2002). Heat transfer and pressure drop correlations for twisted-tape inserts in isothermal tubes: Part I Laminar flows. Journal of Heat Transfer, 121(2), 218-228.

[6] Li, H., & Groll, E. A. (2005). Impact of enhanced surfaces on performance of finned-tube heat exchangers. International Journal of Heat and Mass Transfer, 48(12), 2539-2548.

[7] Shah, R. K., & Sekulic, D. P. (2003). Fundamentals of heat exchanger design. John Wiley & Sons.

[8] Saunders, N., Miodownik, A. P., & Powell, R. J. (2010). Aluminum alloys: Structure and properties (3rd ed.). Elsevier.

[9] Zhang, J., Wang, Q., & Sun, H. (2020). Corrosion behavior and thermal performance of aluminum alloys in heat exchanger applications. Materials Science and Engineering: A, 789, 139615.

[10] Hatch, J. E. (1984). Aluminum: Properties and physical metallurgy. ASM International.

[11] Liu, Z., He, X., & Liu, W. (2017). Effect of alloying elements on the microstructure and properties of aluminum alloys. Materials Science and Engineering: A, 682, 206-214.

[12] Niu, Y., Wei, H., & Zhang, X. (2021). Advances in manufacturing and performance of aluminum alloy finned tubes. Materials & Design, 198, 109393.

[13] Patil, P. A., & Bhave, S. M. (2011). Fabrication and evaluation of integral fins in aluminum alloy tubes. International Journal of Advanced Manufacturing Technology, 54(1), 59-66.

[14] Li, Q., Feng, Z., & Chen, H. (2020). Performance evaluation of internal finned tubes using CFD. International Journal of Heat and Mass Transfer, 150, 119300.

[15] Salcı, O. (2023). Fırın sisteminde hidrojen gazı katkılı doğal gaz yakıtlı proses brülörü yanma analizleri ve optimizasyonu (Master's thesis, Trakya Üniversitesi Fen Bilimleri Enstitüsü)

[16] Cengel, Y. A., & Ghajar, A. J. (2014). Heat and Mass Transfer (in SI Units).

[17] ANSYS Fluent 2023R2, Theory guide. July 2023.

[18] Cengel, Y., & Cimbala, J. (2013). Ebook: Fluid mechanics fundamentals and applications (si units). McGraw Hill.